

Matrix Diffusion and Colloid-Facilitated Transport in Fractured Rocks: Model and Parameter Validation

Mavrik Zavarin

May 2, 2002

U.S. Department of Energy

Lawrence
Livermore
National
Laboratory

DISCLAIMER

This document was prepared as an account of work sponsored by an agency of the United States Government. Neither the United States Government nor the University of California nor any of their employees, makes any warranty, express or implied, or assumes any legal liability or responsibility for the accuracy, completeness, or usefulness of any information, apparatus, product, or process disclosed, or represents that its use would not infringe privately owned rights. Reference herein to any specific commercial product, process, or service by trade name, trademark, manufacturer, or otherwise, does not necessarily constitute or imply its endorsement, recommendation, or favoring by the United States Government or the University of California. The views and opinions of authors expressed herein do not necessarily state or reflect those of the United States Government or the University of California, and shall not be used for advertising or product endorsement purposes.

This work was performed under the auspices of the U. S. Department of Energy by the University of California, Lawrence Livermore National Laboratory under Contract No. W-7405-Eng-48.

This report has been reproduced
directly from the best available copy.

Available to DOE and DOE contractors from the
Office of Scientific and Technical Information
P.O. Box 62, Oak Ridge, TN 37831
Prices available from (423) 576-8401
<http://apollo.osti.gov/bridge/>

Available to the public from the
National Technical Information Service
U.S. Department of Commerce
5285 Port Royal Rd.,
Springfield, VA 22161
<http://www.ntis.gov/>

OR

Lawrence Livermore National Laboratory
Technical Information Department's Digital Library
<http://www.llnl.gov/tid/Library.html>

**Matrix Diffusion and Colloid-Facilitated Transport in Fractured Rocks: Model and
Parameter Validation**

Mavrik Zavarin

Lawrence Livermore National Laboratory
Livermore, California

Prepared for the Underground Test Area Project
U. S. Department of Energy
National Nuclear Security Administration
Nevada Operations Office

Final Report
May 2002

TABLE OF CONTENTS

1 INTRODUCTION.....	1
2 EVALUATION OF TRACER STUDIES AND DETERMINATION OF EFFECTIVE DIFFUSION COEFFICIENTS	1
2.1 INTRODUCTION TO EXPERIMENTAL DATA OF REIMUS ET AL. (2000A)	1
2.2 ALTERNATIVE APPROACH TO MODELING DATA OF REIMUS ET AL. (2000A) FOR INCLUSION IN HST SIMULATIONS	2
2.2.1 <i>Diffusion cell experiments</i>	3
2.2.2 <i>Flow-through experiments</i>	4
2.2.3 <i>Simultaneous model fitting to diffusion cell and flow-through data</i>	4
2.3 SUMMARY OF TRACER STUDIES	5
3 EVALUATION OF COLLOID-FACILITATED PLUTONIUM TRANSPORT IN FRACTURED TUFF COLUMN EXPERIMENTS	5
3.1 INTRODUCTION TO EXPERIMENTAL DATA OF REIMUS ET AL. (2000B)	5
3.2 SIMULATION OF EXPERIMENTAL DATA OF REIMUS ET AL. (2000B)	6
3.2.1 <i>Sorbing Minerals</i>	7
3.2.2 <i>Colloids and the redox state of plutonium</i>	9
3.3 BREAKTHROUGH RESULTS FOR SMECTITE COLLOID (CA-MONTMORILLONITE AND OTAY-MONTMORILLONITE) FLOW-THROUGH EXPERIMENTS	10
3.4 BREAKTHROUGH RESULTS FOR SILICA COLLOID FLOW-THROUGH EXPERIMENTS....	12
3.5 SUMMARY OF COLLOID-FACILITATED PLUTONIUM TRANSPORT STUDIES	13
4 EVALUATION OF CHESHIRE HST FRACTURE-FLOW MODELING.....	14
4.1 MODELING SCENARIOS	14
4.2 RESULTS AND MODEL COMPARISONS	16
4.3 SUMMARY OF CHESHIRE HST FRACTURE-FLOW MODELING	18
5 CONCLUSIONS	19
6 RECOMMENDATIONS	20
7 REFERENCES	20
8 ACKNOWLEDGEMENTS.....	23

LIST OF FIGURES

FIGURE 1. CORRELATION DIAGRAM BETWEEN EXPERIMENTALLY DETERMINED D_E (DIFFUSION CELL DATA) AND PREDICTED D_E BASED ON ARCHIE'S LAW AND $M = 1.7$. RED COLOR DENOTES DUPLICATE ANALYSES OF SUB-SAMPLES FROM THE PM2 4177 FRACTURED ROCK SAMPLE.	26
FIGURE 3. GRID USED TO SIMULATE FRACTURE FLOW UTILIZING DATA FROM FRACTURED TUFF FLOW-THROUGH COLUMNS OF REIMUS ET AL. (2000A). GRID BLOCKS NOT TO SCALE.	28
FIGURE 4. STRATIGRAPHIC UNIT, LITHOLOGY, AND ALTERATION OF TUFFS FROM UE-20C. CIRCLE INDICATES ZONE FROM WHICH FRACTURED TUFF SAMPLES WERE TAKEN FOR EXPERIMENTS REPORTED IN REIMUS ET AL. (2000B). DATA FROM WARREN ET AL. (2000)	29
FIGURE 5. RELATIVE FRACTION OF PLUTONIUM OXIDATION STATES IN J-13 TYPE WATER AS A FUNCTION OF $O_2(G)$ FUGACITY (BARS) UNDER EQUILIBRIUM CONDITIONS.	30
FIGURE 6. EXPERIMENT 1A (FIGURE 2-11 IN REIMUS ET AL., 2000B). DATA POINTS ARE BREAKTHROUGH DATA FOR TRITIUM (BLACK), PLUTONIUM (BLUE), AND CLAY COLLOIDS (RED). SOLID LINES ARE SIMULATION RESULTS USING IDEALIZED DIFFUSION COEFFICIENT () AND $\text{LOG}(D_E) \pm 0.5$ () AT $O_2(G)$ FUGACITY = 10^{-15} BARS (INSET: LOG-SCALE PLUTONIUM BREAKTHROUGH).	30
FIGURE 7. EXPERIMENT 1A (FIGURE 2-11 IN REIMUS ET AL., 2000B). DATA POINTS ARE BREAKTHROUGH DATA FOR PLUTONIUM (BLUE). SOLID LINES ARE SIMULATION RESULTS USING IDEALIZED DIFFUSION COEFFICIENT () AT $O_2(G)$ FUGACITY = 10^{-7} BARS (LIGHT BLUE) AND 10^{-15} BARS (BLUE) AND $\text{LOG}(D_E) \pm 0.5$ ().	31
FIGURE 8. EXPERIMENT 1B (FIGURE 2-12 IN REIMUS ET AL., 2000B). DATA POINTS ARE BREAKTHROUGH DATA FOR TRITIUM (BLACK), PLUTONIUM (BLUE), AND CLAY COLLOIDS (RED). SOLID LINES ARE SIMULATION RESULTS USING IDEALIZED DIFFUSION COEFFICIENT () AND $\text{LOG}(D_E) \pm 0.5$ () AT $O_2(G)$ FUGACITY = 10^{-15} BARS (INSET: LOG-SCALE PLUTONIUM BREAKTHROUGH).	31
FIGURE 9. EXPERIMENT 2A (FIGURE 2-13 IN REIMUS ET AL., 2000B). DATA POINTS ARE BREAKTHROUGH DATA FOR TRITIUM (BLACK), PLUTONIUM (BLUE), AND CLAY COLLOIDS (RED). SOLID LINES ARE SIMULATION RESULTS USING IDEALIZED DIFFUSION COEFFICIENT () AND $\text{LOG}(D_E) \pm 0.5$ () AT $O_2(G)$ FUGACITY = 10^{-15} BARS (INSET: LOG-SCALE PLUTONIUM BREAKTHROUGH).	32
FIGURE 10. EXPERIMENT 2B (FIGURE 2-14 IN REIMUS ET AL., 2000B). DATA POINTS ARE BREAKTHROUGH DATA FOR TRITIUM (BLACK), PLUTONIUM (BLUE), AND CLAY COLLOIDS (RED). SOLID LINES ARE SIMULATION RESULTS USING IDEALIZED DIFFUSION COEFFICIENT () AND $\text{LOG}(D_E) \pm 0.5$ () AT $O_2(G)$ FUGACITY = 10^{-15} BARS (INSET: LOG-SCALE PLUTONIUM BREAKTHROUGH).	32
FIGURE 11. EXPERIMENT 5A (FIGURE 2-19 IN REIMUS ET AL., 2000B). DATA POINTS ARE BREAKTHROUGH DATA FOR TRITIUM (BLACK), PLUTONIUM (BLUE), AND CLAY COLLOIDS (RED). SOLID LINES ARE SIMULATION RESULTS USING IDEALIZED DIFFUSION COEFFICIENT () AND $\text{LOG}(D_E) \pm 0.5$ () AT $O_2(G)$ FUGACITY = 10^{-15} BARS (INSET: LOG-SCALE PLUTONIUM BREAKTHROUGH).	33

FIGURE 12. EXPERIMENT 5B (FIGURE 2-20 IN REIMUS ET AL., 2000B). DATA POINTS ARE BREAKTHROUGH DATA FOR TRITIUM (BLACK), PLUTONIUM (BLUE), AND CLAY COLLOIDS (RED). SOLID LINES ARE SIMULATION RESULTS USING IDEALIZED DIFFUSION COEFFICIENT (——) AND $\text{LOG}(D_E) \pm 0.5$ (——) AT $\text{O}_2(\text{G})$ FUGACITY = 10^{-15} BARS (INSET: LOG-SCALE PLUTONIUM BREAKTHROUGH).	33
FIGURE 13. EXPERIMENT 6A (FIGURE 2-21 IN REIMUS ET AL., 2000B). DATA POINTS ARE BREAKTHROUGH DATA FOR TRITIUM (BLACK), PLUTONIUM (BLUE), AND CLAY COLLOIDS (RED). SOLID LINES ARE SIMULATION RESULTS USING IDEALIZED DIFFUSION COEFFICIENT (——) AND $\text{LOG}(D_E) \pm 0.5$ (——) AT $\text{O}_2(\text{G})$ FUGACITY = 10^{-15} BARS (INSET: LOG-SCALE PLUTONIUM BREAKTHROUGH).	34
FIGURE 14. EXPERIMENT 6B (FIGURE 2-22 IN REIMUS ET AL., 2000B). DATA POINTS ARE BREAKTHROUGH DATA FOR TRITIUM (BLACK), PLUTONIUM (BLUE), AND CLAY COLLOIDS (RED). SOLID LINES ARE SIMULATION RESULTS USING IDEALIZED DIFFUSION COEFFICIENT (——) AND $\text{LOG}(D_E) \pm 0.5$ (——) AT $\text{O}_2(\text{G})$ FUGACITY = 10^{-15} BARS (INSET: LOG-SCALE PLUTONIUM BREAKTHROUGH).	34
FIGURE 15. EXPERIMENT 3A (FIGURE 2-15 IN REIMUS ET AL., 2000B). DATA POINTS ARE BREAKTHROUGH DATA FOR TRITIUM (BLACK), PLUTONIUM (BLUE), AND SILICA COLLOIDS (RED). SOLID LINES ARE SIMULATION RESULTS USING IDEALIZED DIFFUSION COEFFICIENT (——) AND $\text{LOG}(D_E) \pm 0.5$ (——) AT $\text{O}_2(\text{G})$ FUGACITY = 10^{-15} BARS....	35
FIGURE 16. EXPERIMENT 4A (FIGURE 2-17 IN REIMUS ET AL., 2000B). DATA POINTS ARE BREAKTHROUGH DATA FOR TRITIUM (BLACK), PLUTONIUM (BLUE), AND SILICA COLLOIDS (RED). SOLID LINES ARE SIMULATION RESULTS USING IDEALIZED DIFFUSION COEFFICIENT (——) AND $\text{LOG}(D_E) \pm 0.5$ (——) AT $\text{O}_2(\text{G})$ FUGACITY = 10^{-15} BARS (INSET: LOG-SCALE PLUTONIUM BREAKTHROUGH).	35
FIGURE 17. FIGURE 6.12 OF PAWLOSKI ET AL. (2001) SHOWING THE CONCEPTUAL MODEL USED TO DEFINE THE NATURE OF EFFECTIVE POROSITY AND THE INTERACTION OF RADIONUCLIDES WITH FRACTURE-LINING MINERALS AND MATRIX MINERALS.....	36
FIGURE 18. SCHEMATIC OF THREE TYPES OF FLOW SIMULATIONS PERFORMED USING THE CRUNCH CODE.....	37
FIGURE 19. BREAKTHROUGH OF PLUTONIUM AND A TRACER IN THE 1D SIMULATIONS PRESENTED IN FIGURE I.7 OF PAWLOSKI ET AL. (2001).....	38
FIGURE 20. BREAKTHROUGH OF TRACER IN THE 1D SIMULATION PRESENTED IN FIGURE I.7 OF PAWLOSKI ET AL. (2001) (RED) AND CASE A SIMULATION (BLACK). LINEAR SCALE INDICATES BREAKTHROUGH AT 5 YEARS.	38
FIGURE 21. BREAKTHROUGH OF PLUTONIUM IN THE 1D SIMULATION PRESENTED IN FIGURE I.7 OF PAWLOSKI ET AL. (2001) (RED) AND CASE A SIMULATION (BLACK).....	39
FIGURE 22. BREAKTHROUGH OF TRITIUM FOR CASE A (YELLOW), CASE B (BLACK), CASE C (PINK).	39
FIGURE 23. BREAKTHROUGH OF PLUTONIUM FOR CASES A (COLORED THICK LINES), B (BLACK LINES), AND C (COLORED THIN LINES) UNDER CONDITIONS OF $\text{O}_2(\text{G})$ FUGACITY OF 10^{-7} BARS (ORANGE), 10^{-15} BARS (PINK), AND 10^{-15} BARS AND TEN-FOLD INCREASE IN COLLOID REACTIVITY (TURQUOISE). CASE B RESULTS IN BLACK.	40
FIGURE 24. BREAKTHROUGH OF PLUTONIUM IN CASE C IN WHICH $\text{O}_2(\text{G})$ FUGACITY IS 10^{-15} BARS AND COLLOID REACTIVITY INCREASED TEN-FOLD. LIGHT TURQUOISE DATA SHOW THE EFFECT OF UNCERTAINTY IN THE DIFFUSION COEFFICIENT.	40

LIST OF TABLES

TABLE 1. RADIONUCLIDE SORBING MINERAL ABUNDANCES IN THE FRACTURE LININGS AND DEVITRIFIED TUFF USED IN THE SIMULATION OF FRACTURE FLOW EXPERIMENTS OF REIMUS ET AL. (2000B).†	24
TABLE 2. PARAMETERS USED IN SIMULATION OF COLUMN FLOW-THROUGH EXPERIMENTS.	25

1 INTRODUCTION

In this report, we review the results of Reimus et al. (2000a; 2000b) regarding matrix diffusion and colloid-facilitated transport in fractured rock and evaluate the implications of these results on modeling fracture flow at the Nevada Test Site (NTS). In particular, we examine these data in the context of the recent Cheshire hydrologic source term (HST) model results (Pawloski et al., 2001).

This report is divided into several sections. In the first, we evaluate the effective diffusion coefficient (D_e) data reported in Reimus et al. (2000a) for conservative tracer species (^3H , ^{14}C , and ^{99}Tc) and fit a simple effective diffusion model to these data. In the second, we use the fitted effective diffusion model, in conjunction with a surface complexation model, to simulate plutonium-colloid transport and compare model results to data reported in Reimus et al. (2000b). In the third, we evaluate the implications of these data with regards to radionuclide transport through fractures at the field scale and, in particular, with regards to the Cheshire HST model (Pawloski et al., 2001). Finally, we make recommendations regarding future radionuclide transport modeling efforts at the NTS.

2 EVALUATION OF TRACER STUDIES AND DETERMINATION OF EFFECTIVE DIFFUSION COEFFICIENTS

2.1 Introduction to experimental data of Reimus et al. (2000a)

In Reimus et al. (2000a), the diffusion of ^3H , ^{14}C , and ^{99}Tc is examined under two experimental conditions: diffusion cell experiments and fracture flow experiments. A detailed description of the experimental methods is given in Reimus et al. (2000a) and will not be repeated. However, several conclusions from this report are relevant to our discussion here. These are:

- The D_e of ^{14}C varies widely but is generally greater than that of ^3H and ^{99}Tc in diffusion cell experiments.
- ^{14}C and ^{99}Tc may react with matrix minerals to some degree resulting in retardation.
- Matrix diffusion showed only a slight positive correlation with matrix porosity and matrix permeability.

These conclusions suggest that (1) the three tracers do not all behave conservatively and (2) that predicting their behavior based on matrix porosity or permeability will involve large uncertainties.

If behaving conservatively, the D_e for the three tracers should follow the same order as their respective diffusion coefficients in free water ($2.24 \times 10^{-5} > 1.48 \times 10^{-5} > 1.19 \times 10^{-5}$ cm²/s for ³H₂O, TcO₄⁻, and HCO₃⁻, respectively (Mills and Lobo, 1989)).¹ This order is not observed in Reimus et al. (2000a). ¹⁴C and ⁹⁹Tc retardation may be one factor affecting D_e but it does not fully explain the observed behavior.

The correlation of D_e with matrix porosity and permeability is often used to develop a predictive model for diffusion. Since the data in Reimus et al. (2000a) correlate only slightly with porosity and permeability, predicted ³H, ¹⁴C, and ⁹⁹Tc D_e based on model fits to these data will inevitably involve large uncertainties. These uncertainties stem from a combination of experimental method and complex behavior of diffusing tracers, as will be discussed in this report.

Based on ³H diffusion cell data and earlier pentafluorobenzoate data, Reimus et al. (2000a) proposed the following empirical equation to predict D_e :

$$\text{Log}D_e(\text{cm}^2/\text{s}) = -3.49 + 1.38 \times \phi + 0.165 \times \text{Log}k(m^2) \quad (1)$$

with 95% confidence intervals:

$$\begin{aligned} \text{Intercept: } & -3.49 \pm 1.69 \\ \text{Coefficient for porosity: } & 1.38 \pm 1.45 \\ \text{Coefficient for Log permeability: } & 0.165 \pm 0.09^2 \end{aligned}$$

where ϕ is the matrix porosity, and k is the matrix permeability. A simultaneous fit to all diffusion data in Reimus et al. (2000a) was not reported. Nevertheless, the confidence intervals for the parameters in Equation (1) suggest that predicting D_e based on an empirical fit to porosity and permeability data will involve large uncertainties. In fact, the large uncertainty in the predicted D_e does not justify the use of anything but a rudimentary predictive model. In the following section, we fit a simpler effective diffusion model based solely on matrix porosity to the ³H, ¹⁴C, and ⁹⁹Tc diffusion data presented in Reimus et al. (2000a). We also estimate the uncertainty in our predictive model. Later, we show that the large uncertainty in predicted D_e has little effect on our Cheshire HST simulations. Thus, the uncertainty in predicting D_e may not necessarily result in large uncertainties in radionuclide transport predictions.

2.2 Alternative approach to modeling data of Reimus et al. (2000a) for inclusion in HST simulations

The effective diffusion of a species in a porous material can be defined in the following manner:

¹ We assume that ion exclusion phenomena have only a secondary effect on diffusion.

² Equation 1 and confidence intervals were taken from the final report submitted by Reimus et al. in January, 2002.

$$D_e = D_v \frac{\phi \delta}{\tau^2} \quad (2)$$

where the free diffusion of a species in water (D_v) is adjusted by the porosity of the medium (ϕ), the constrictivity of the medium (δ), and the tortuosity of the medium (τ). Because the constrictivity and tortuosity of a medium are difficult to separate experimentally, simpler forms of this equation, such as Archie's Law, have been proposed:

$$D_e = D_v \phi^m \quad (3)$$

where m , defined as the “cementation exponent”, ranges between 1.3 and 2.5 (Dullien, 1979). Below, we model the diffusion data for the three radionuclides reported in Reimus et al. (2000a) using Archie's Law.

2.2.1 Diffusion cell experiments

Reimus et al. (2000a) reported on 33 diffusion cell experiments using ^3H . These data were fit to Equation (3) by optimizing the value of m and minimizing the difference between the logarithm of the experimentally determined and predicted D_e (Figure 1). The least squares fit to Archie's Law results in $m = 1.7$, which is in agreement with the previously established range (1.3 to 2.5, Dullien, 1979). However, the correlation between the experimentally determined and predicted D_e is weak (note spread in Figure 1), consistent with the conclusion in Reimus et al. (2000a). Importantly, for six diffusion experiments using the same tuff (PM2 4177, highlighted in red in Figure 1), the range of experimentally determined D_e for ^3H (± 2 standard deviations) was 5.3×10^{-7} to 3.6×10^{-6} cm^2/s (a range of a factor of 7).³ The uncertainty in experimentally determined D_e for six diffusion cell experiments using tuff from the same location with identical matrix porosity (and nearly identical permeability) clearly indicates that a poor correlation between experimentally derived and predicted D_e will invariably exist. The uncertainty is derived most likely from a combination of experimental method and complex behavior of tracers in heterogeneous rock.

The diffusion cell data for ^{14}C and ^{99}Tc show even less correlation with porosity than ^3H . Uncertainty in the D_e of ^{14}C and ^{99}Tc for six diffusion experiments using the same tuff (PM2 4177) is also large. The two standard deviation range for ^{14}C and ^{99}Tc D_e is 4.2×10^{-7} to 1.2×10^{-5} , and 6.4×10^{-8} to 1.2×10^{-5} cm^2/s , respectively (ranges of a factor of 29 and 190, respectively). Again, based on these data, a poor correlation between experimentally derived and predicted D_e will invariably exist.

³ All average and standard deviations for diffusion coefficients were calculated using the logarithm of the diffusion coefficients.

Regardless of the form of the equation used to calculate D_e , in theory, the D_e of a tracer should correlate with porosity. However, the data of Reimus et al. (2000a) show only a weak correlation. Several reasons for the poor correlation can be envisioned. First, the range of porosities examined in Reimus et al. (2000a) is rather small (5 to 35%) which makes the correlation difficult to observe.⁴ Second, microfracturing and spatial variation in porosity may result in multiple diffusion paths with varying diffusivities. Third, it is clear from the diffusion cell experiments that the measured D_e varies widely for multiple experiments using the same tuff. Either the sample is altered between experiments or the experimental method itself is subject to large uncertainties. Problems such as biofouling were suggested in Reimus et al. (2000a) to explain some of the data variability. The combination of these factors results in poor correlation between experimentally determined D_e and porosity and, in turn, experimentally determined and predicted D_e s.

2.2.2 Flow-through experiments

Reimus et al. (2000a) reported on 33 flow-through experiments using 7 flow-through columns. Most experiments were performed using ^3H , ^{14}C , and ^{99}Tc tracers injected simultaneously. In all cases, the experimentally determined retardation factor for all three tracers is close to 1. Unlike the diffusion cell experiments, retardation does not seem to play a significant role in mass transfer from the fracture to the matrix.

As in the case of diffusion cell experiments, the differences in D_v among the three tracers are small compared to the uncertainty in experimentally determined D_e . In flow-through experiments, breakthrough should follow the order HCO_3^- , TcO_4^- , ^3HHO based on the order of increasing D_v . Flow-through experiments in which all three tracers were injected simultaneously (see Reimus et al. (2000a), Appendix C) sometimes showed distinct differences in the breakthrough of the three tracers but the order of radionuclide breakthrough varied between experiments. As in the case of the diffusion cell experiments, any subtle differences in D_v of the three tracers is not resolvable given the large variability in experimentally determined D_e .

2.2.3 Simultaneous model fitting to diffusion cell and flow-through data

In Figure 2, we present the best fit of the Archie's Law model to the entire D_e data set reported in Reimus et al. (2000a). The correlation results are presented in the form of matrix diffusion mass transfer coefficients ($\phi D_e^{1/2} R^{1/2}$).⁵ Matrix diffusion mass transfer coefficients were used in Reimus et al. (2000a) to present both the diffusion cell and flow-through experiments. We use this same format here. The best fit to the data is achieved with $m = 1.3$ which lies within the previously estimated range for this exponent (Dullien, 1979). Notwithstanding the large uncertainties in experimentally determined

⁴ For example, assuming a cementation exponent of 1.5 and a porosity range of 5 to 35%, the effective diffusion would span an order of magnitude. If rocks with 1% porosity were available, effective diffusion would span two orders of magnitude (e.g. Sato, 1999).

⁵ In our analysis, we assume that the retardation factor, R , is equal to 1. Thus, the matrix diffusion mass transfer coefficient can be simplified to $\phi D_e^{1/2}$.

D_e , Equation (3) is able to predict D_e reasonably well. The correlation between predicted and measured mass transfer coefficients in all flow-through experiments and the ^3H diffusion cell experiments is reasonably good. Most data fall within a range of uncertainty of $\text{Log}(D_e) \pm 0.5$, as shown in Figure 2. This range of variability is consistent with the D_e uncertainty (two standard deviation) measured for ^3H diffusion cell experiments in which a set of six experiments using the same tuff were used (Section 2.2.1). In the case of ^{14}C and ^{99}Tc diffusion cell data, the correlation between experimentally determined and predicted D_e is quite poor. These experiments were subject to several problems including biofouling and possible TcO_4^- reduction. The non-ideal behavior of these tracers was acknowledged in Reimus et al. (2000a); a retardation factor had to be included in their model to extract D_e from the experimental data.

2.3 Summary of tracer studies

We find that the large uncertainty in experimentally determined D_e stems most likely from a combination of experimental method and complex behavior of diffusing tracers and medium. Problems such as biofouling have been suggested in Reimus et al. (2000a). The large uncertainties in experimentally determined D_e will limit the accuracy of any predictive model for D_e . This uncertainty, particularly for the diffusion cell experiments, does not justify the use of anything but a rudimentary predictive model. We fit the simple Archie's Law model based solely on porosity to the complete set of experimentally determined D_e data for all three tracers (^3H , ^{14}C , and ^{99}Tc) reported in Reimus et al. (2000a). When all experimentally determined data are used, the model fit is best with $m = 1.3$. This value is consistent with published ranges for the cementation exponent. The correlation in the case of flow-through experiments and ^3H diffusion cell experiments is reasonable. The majority of the data fall within a nominal D_e uncertainty of $\text{Log}(D_e) \pm 0.5$. In the case of ^{14}C and ^{99}Tc diffusion cell data, the correlation between experimentally determined and predicted D_e is very weak. The significant uncertainty in predicting D_e must be addressed in reactive transport simulations. In the following section, we evaluate the data reported in Reimus et al. (2000b) for colloid-facilitated plutonium transport and use the modeling results from this section to assign D_e and an estimated uncertainty of $\text{Log}(D_e) \pm 0.5$.

3 EVALUATION OF COLLOID-FACILITATED PLUTONIUM TRANSPORT IN FRACTURED TUFF COLUMN EXPERIMENTS

3.1 Introduction to experimental data of Reimus et al. (2000b)

Recent observations of colloid-facilitated transport of radionuclides at the Nevada Test Site (Kersting et al., 1999) have prompted investigations into colloid-facilitated transport in fractured tuffs on Pahute Mesa. Reimus et al. (2000b) examined the reactive transport of plutonium through fractured tuff at Pahute Mesa. A total of 12 flow-through experiments were performed, each of which involved both plutonium and tritium (^3H). Tritium was used to compare tracer breakthrough with the more complex behavior of

plutonium. In each experiment, plutonium associated with either silica or smectite colloids was injected in one of two fractured columns, at a particular fluid flow rate, and using either synthetic Pahute Mesa groundwater or natural water from well U-20ww. The transport was evaluated by sampling effluent and analyzing for plutonium, colloids, and tritium. Some characterization of the fracture-lining mineralogy and tuff mineralogy was accomplished. A post-mortem evaluation of plutonium and colloid associations in the column was attempted but will not be discussed here. A small number of batch sorption/desorption experiments were also performed to evaluate plutonium interaction with silica and smectite colloids.

Some concluding remarks from Reimus et al. (2000b) are worth noting. Reimus et al. (2000b) suggested that it is unlikely that Pu(V)^6 would travel in significant quantities over significant distances when sorbed to smectite or silica colloids. They suggested that the manganese-oxide-dominated fracture-lining surfaces may out-compete colloids for sorption of plutonium. This seems to contradict the observations of Kersting et al. (1999) with regards to colloid-facilitated plutonium mobility. However, aqueous plutonium concentrations observed by Kersting et al. (1999) were many orders of magnitude lower than those used in Reimus et al. (2000b). The seeming contradiction cannot, therefore, be resolved.

3.2 Simulation of experimental data of Reimus et al. (2000b)

We simulated the cylindrical fractured rock column flow-through experiment data reported in Reimus et al. (2000b) using a 2D parallel plate half-fracture reactive transport model. A 25 by 12 2D grid was used (Figure 3). In the transport model, flow was confined to the fracture while aqueous species were allowed to diffuse between the flowing fracture, the fracture-lining, and the matrix. Colloids were isolated within the fracture and traveled *in the absence of any filtration or retardation mechanisms*. This simplified colloid model was used here for consistency with the Cheshire HST model (Pawloski et al., 2001). However, it is important to note that, based on this assumption, simulation results of colloid breakthrough were not expected to be consistent with the data in Reimus et al. (2000b). Column dimensions and fluid flow rates were taken directly from measured values. Fracture apertures were taken from model parameters reported in Reimus et al. (2000b) based on fits to the tritium breakthrough curves. D_e s were calculated using Archie's Law and $m = 1.3$. No physical dispersion was used although numerical dispersion in our modeling code is quite significant (see Section 4).

The method used here to simulate the reactivity of plutonium in a fracture flow environment is based on the reactive transport methodology used in the Cheshire HST model (Pawloski et al., 2001). GIMRT (the global implicit option of the CRUNCH code) was used to model reactive transport. This code allows for a detailed description of

⁶ Significant data in the literature suggest that Pu(V) is likely to reduce to Pu(IV) upon sorption to mineral surfaces including montmorillonite and silica. It is, therefore, likely that these flow-through experiments were not specific to Pu(V) but were, in fact, composed of a mixture of Pu(V) and Pu(IV) as well as small quantities of Pu(VI) and Pu(III) .

geochemistry. Reactions accounted for by the CRUNCH code can include: surface complexation, ion exchange, mineral dissolution/precipitation, radionuclide decay/ingrowth, various kinetic reactions, and other processes. For additional information on the CRUNCH code, see Steefel (2000) and Giambalvo et al. (2001).

For the single fracture simulations used to evaluate the experimental data of Reimus et al. (2000b), the following geochemical reactions were taken into account:

- plutonium redox
- plutonium aqueous speciation
- plutonium surface complexation to silica
- plutonium surface complexation to iron oxide
- plutonium surface complexation to calcite
- plutonium surface complexation to smectite.⁷

There was no need to account for mineral precipitation/dissolution reactions or radionuclide decay due to the short time frame and ambient conditions of the fracture flow experiment. Ion exchange of plutonium is believed to be rather insignificant compared to surface complexation due to the strong complexation of plutonium in solution under ambient NTS groundwater conditions as well as steric hindrance. For a detailed explanation of surface complexation and aqueous speciation and the constants used, see Zavarin and Bruton (2000a, 2000b) and Pawloski et al. (2001).

3.2.1 Sorbing Minerals

To properly simulate reactive transport in these fractures, the radionuclide sorbing mineral abundances in the fracture linings, fractured tuff, and colloids must be known. Only the mineralogy of the colloids was reported in Reimus et al. (2000b).⁸ For modeling purposes, the mineralogy of the tuff and fracture lining had to be estimated from analog samples. The fractured rock used in the column experiments was taken from between 2850 and 2860 feet below ground surface from well UE-20c at Pahute Mesa, NTS (Figure 4; data from Warren et al., 2000). Tuff at this location belongs to the Pahute Mesa lobe of the Topopah Spring Tuff: a partially to moderately welded devitrified tuff. The mineralogy of the tuff and fracture lining could, therefore, be estimated from published data on other devitrified tuffs and lavas at or near Pahute Mesa. The mineralogy of devitrified tuff found at the Cheshire site (devitrified mafic-poor Calico Hills lava) was

⁷ Surface complexation to manganese oxides was not included because these reaction constants are not available. Manganese oxide reactivity is discussed later in this report.

⁸ Mineralogy of the fracture-lining minerals and tuff is planned but was not accomplished in time to be included in the report of Reimus et al. (2000b).

used as an analog for devitrified tuff mineralogy. The fracture-lining mineralogy of devitrified tuffs below the water table at Yucca Mountain was used as an analog for the fracture-lining mineralogy. For a more complete discussion of the mineralogy of devitrified tuffs and associated fracture-lining minerals, as well as a discussion of the strengths and weaknesses of extrapolating mineralogic data from other locations, see Pawloski et al. (2001).

The plutonium-sorbing minerals accounted for in these simulation, along with their abundances and properties are summarized in Table 1.⁹ The mineral abundances, based on analog samples, can be compared to some semi-quantitative mineral abundance information reported in Drellack et al. (1997). Based on the U-20c and UE-20c well Tuff Cone hydrostratigraphic unit data (Topopah Springs tuff belongs to this *hydrostratigraphic* unit), the presence of fracture lining mineral follows the order: iron/manganese oxides > chalcedony > clay > zeolite > calcite (Drellack et al., 1997). The distribution of fracture lining minerals in the U-20c and UE-20c well Welded Tuff Aquifer hydrogeologic unit (Topopah Spring tuff also belongs to this *hydrogeologic* unit) follows that same order. This is in general agreement with our quantitative analog data presented in Table 1.

The reactivity of colloid, fracture-lining, and matrix minerals were based on the volume fraction, density, surface area, reactive site density, and associated reaction constants of the plutonium-sorbing minerals. Reactive site densities and associated surface complexation constants of the plutonium-sorbing minerals are not listed in this report but can be found in Pawloski et al. (2001).

A significant limitation to the list of sorbing minerals used in the surface complexation model (Table 1) is the absence of manganese oxides. Analysis of devitrified tuffs below the water table at Yucca Mountain showed that manganese oxides would comprise a large fraction of the fracture-lining mineralogy. However, the limited published sorption data did not allow for the incorporation of manganese oxides into a surface complexation model. Information on the sorptive behavior of manganese oxides for plutonium is sparse (Keeney-Kennicutt and Morse, 1985; Vaniman et al., 1995; Duff et al., 1999). Keeney-Kennicutt and Morse (1985) found that δ -MnO₂ was the weakest sorber out of the group of minerals they examined (goethite, aragonite, calcite, δ -MnO₂). Vaniman et al. (1995) found that a more general association of plutonium with smectite can be found for Yucca Mountain tuffs, though oxide minerals (including manganese and iron oxides) can retain plutonium very strongly when they are present. Duff et al. (1999) examined Yucca Mountain tuff using x-ray microprobe techniques and found that plutonium was predominantly associated with ranceite (a manganese oxide) and smectite. The significant presence of manganese oxides in the flow-through columns was discussed in Reimus et al. (2000b). It was also observed at the Cheshire site (Pawloski et al., 2001).

⁹ Note that those minerals that participate primarily in ion exchange (zeolite, mica) were not included in our modeling of the fracture flow columns since plutonium does not participate significantly in ion exchange reactions. In the Cheshire near-field modeling, many other radionuclides were modeled and their ion exchange with zeolite and mica was included.

The absence of manganese oxides in these fracture flow simulations results in a more conservative estimate of plutonium sorption to fracture-lining minerals, but may not dramatically alter the results of these simulations since other strong plutonium sorbing minerals (e.g. iron oxide) are included in the model.

3.2.2 Colloids and the redox state of plutonium

Reimus et al. (2000b) measured the colloid load in solution as particles/mL (Table 2) but the surface area of the colloids was not reported. Thus, the reactivity of the colloids could not be directly calculated. However, transmission electron microscopic (TEM) images (Reimus et al., 2000b) indicate that the clay and silica particle sizes are ~500 nm and ~100 nm, respectively. Using the reactive site densities of our surface complexation model (Pawloski et al., 2001) and assuming a surface area based on spherical particles, we can estimate a colloid reactive site concentration of $\sim 10^{-6}$ mol/L (see Table 2 for specific concentrations for each simulation). However, the reactive site concentration estimate based on spherical particle geometry is likely to result in a low surface area estimate since real colloid particles are likely to have more complex topography which could significantly increase their reactive surface area.

The predicted Pu surface complexation to colloids using estimated reactive surface areas was compared to results of batch sorption experiments described in Reimus et al. (2000b). Two parameters had to be adjusted in our model to fit the measured batch sorption data: fugacity of O₂(g) and colloid reactive surface area. The fugacity of O₂(g) can be used to adjust plutonium sorption because the concentration of Pu(IV) relative to Pu(V) in solution affects net plutonium sorption. This is because Pu(IV) is a much stronger sorber than Pu(V). However, increasing the relative concentration of Pu(IV) increases net plutonium sorption to all sorbing minerals including colloid, fracture-lining, and matrix minerals. Thus a complex interplay between plutonium sorption to colloids and fracture lining and matrix minerals controls transport. The colloid reactive surface area was also used to adjust plutonium sorption to colloids. In this case, increasing the colloid reactive surface area increases the sorption strength of the colloids *relative* to the fracture lining and matrix minerals (see Table 2 for simulation details). Since the surface area of the colloids was not reported in Reimus et al. (2000b), there is significant uncertainty in our estimated colloid reactive surface areas. To match the batch sorption data, the colloid surface area in the model needed to be increased by a factor of ~50 from the initial TEM-based estimate. This is not altogether unreasonable given the uncertainty of our TEM-based estimate. A detailed discussion of O₂(g) fugacity adjustments follows.

Measured data suggest that plutonium is rarely found in redox equilibrium in solution and that significant quantities of Pu(IV) can be present in groundwater (Nitsche et al., 1993; 1994). Pu(V) was found to be the dominant oxidation state of plutonium in J-13 type¹⁰ waters (Nitsche et al., 1993; 1994). However, when a Pu(V) solution is added to J-13 type or NaClO₄ water, it is quickly transformed to a mixture of 70% Pu(V) and 30%

¹⁰ J-13 type waters refers to low ionic strength sodium carbonate waters typically found at Yucca Mountain and the Nevada Test Site. J-13 refers to a production well located at Yucca Mountain.

Pu(III), Pu(IV), and Pu(VI) (Nitsche and Edelstein, 1985). It is likely that this same reaction occurred in the solutions of Reimus et al. (2000b). It is also likely that the reaction of Pu(V) with colloid surfaces further alters the final redox state of plutonium in solution and on the solid. For example, it has been observed that Pu(V) is a relatively weak sorber while Pu(IV) is a strong sorber, particularly when smectite is the sorbing mineral (Sanchez, 1983). In fact, the oxidation state of sorbed plutonium can be dominated by Pu(IV) even when the aqueous fraction is Pu(V)-dominated (Sanchez, 1983).

Furthermore, the redox state of plutonium is not simply a thermodynamic equilibrium issue. Factors such as radiolysis and disproportionation also affect the final redox state of plutonium in solution (or on the solid). At present, there is insufficient information on the many plutonium redox transformation pathways to effectively account for them in a comprehensive manner. Instead, the oxidation state of plutonium is controlled in these simulations by assuming thermodynamic equilibrium and establishing an “effective” $O_2(g)$ fugacity. The fugacity of $O_2(g)$ can then be used to “tune” plutonium redox to an oxidation state distribution consistent with experimental data. Thus, the stated $O_2(g)$ fugacity should not be taken as the actual equilibrium redox state of NTS waters but simply as a reference to the distribution of plutonium redox states in solution.

In Figure 5, the equilibrium redox states of plutonium are shown as a function of $O_2(g)$ fugacity. In Cheshire HST simulations, an O_2 fugacity of 10^{-7} bars was chosen because it resulted in Pu(V) dominance in solution while minimizing the concentration of Pu(IV). This resulted in weak sorption of plutonium to fracture-lining minerals. This also resulted in weak sorption of plutonium to colloids. Thus colloids played virtually no role in plutonium transport in Cheshire HST simulations. A lower average oxidation number of plutonium would increase sorption to colloids. However, it would also result in increased sorption to fracture-lining and matrix minerals. This will be further discussed in Section 4 of this report. To effectively fit the batch sorption data of Reimus et al. (2000b), an $O_2(g)$ fugacity of 10^{-15} bars was necessary. This O_2 fugacity is used to simulate the oxidation states of plutonium in the flow-through experiments of Reimus et al. (2000b) as well. For comparison, reactive transport simulations using an $O_2(g)$ fugacity of 10^{-7} bars are also presented.

3.3 Breakthrough results for smectite colloid (Ca-montmorillonite and Otay-montmorillonite) flow-through experiments

Breakthrough data and simulation results for plutonium and tritium transport in smectite colloid flow-through experiments are shown in Figures 6 to 14. The parameters used to model each flow-through experiment are listed in Table 2. In general, simulation results match tritium breakthrough data within the limits of uncertainty in D_e and without any adjustment of model parameters.¹¹

¹¹ While the effect of D_e uncertainty was examined in our simulations, uncertainties in the surface complexation constants, fracture apertures, and other parameters were not. An analysis of these uncertainties would certainly increase the range of breakthrough presented in Figures 6 to 16.

Two parameters were adjusted to fit plutonium breakthrough data: $O_2(g)$ fugacity and colloid reactive surface area, as described earlier. Additional changes to model parameters could have permitted an even better model fit to data. However, a primary goal of this report was to evaluate whether the model parameters used in the Cheshire HST model could fit these fracture flow experiment data. As such, the number of fitting parameters was kept to a minimum.

The tailing in plutonium breakthrough data could not be properly fit.¹² The tailing in plutonium correlates with the tailing in the colloid breakthrough. This is not unexpected given the strong association of plutonium with colloids. Tailing in the colloid breakthrough resulted from significant colloid filtration in these experiments. As will be discussed below, the transport behavior of colloids was modeled in a rudimentary fashion (no filtration) and was not expected to match breakthrough data. Since tailing was not predicted for colloids in our model, it was not predicted for plutonium.

Importantly, the sorption reactions in our model were equilibrium reactions (i.e. no kinetic behavior). The reasonably good fit of simulation results to the breakthrough data seems to indicate that sorption and desorption kinetics may be fast enough to be relatively unimportant with regards to plutonium transport in these experiments. Reimus et al. (2000b) found that the K_d for plutonium maximum sorption to the various colloids in the two fluids used (batch sorption experiments) ranged from 1.2×10^4 to 8.6×10^4 mL/g.¹³ During the initial period of desorption (1 hour to 1 day), K_{ds} ranged from 6.2×10^3 to 3.6×10^4 mL/g. If plutonium desorption rates were very slow, one would expect that the initial *desorption* K_{ds} would be significantly higher than the maximum *sorption* K_{ds} . The results suggest that the desorption rates, although not necessarily as fast as sorption rates, are relatively fast, and should play only a minor role in these plutonium transport experiments. Moreover, at the scale of flow velocities and residence times observed in the field, the difference in sorption and desorption rates observed in Reimus et al. (2000b) is likely to have a negligible effect on overall transport.

As mentioned earlier, the predicted colloid breakthrough does not match experimental data. Reimus et al. (2000b) observed that only a fraction of the colloids (10-90%) was collected at the downstream boundary and concluded that filtration significantly retarded colloid breakthrough. Colloid filtration was not included in the simulations presented in this report. If colloid filtration were included, plutonium breakthrough would be attenuated and the match to plutonium breakthrough data would be compromised. However, this would, at most, decrease the plutonium breakthrough concentration by an order of magnitude. To match both the plutonium breakthrough and colloid breakthrough, colloid filtration would have to be invoked along with plutonium sorption/desorption kinetics, reduced plutonium diffusivity, and/or reduced plutonium

¹² The detection limit of the breakthrough data for plutonium is approximately $C/Co = 0.005$. Thus, on the Log-scale plots, much of the tailing is at the detection limit of the data.

¹³ K_d , the distribution coefficient, is defined as the ratio of mol sorbed radionuclide per gram solid to mol aqueous (free) radionuclide per mL solution. In this case, the solid is the colloid material.

sorption to fracture-lining and matrix minerals. This suggests that plutonium desorption kinetics could play some role in these plutonium breakthrough results. However, other processes may also affect downstream plutonium breakthrough in a similar way. Regardless, the equilibrium modeling results and the estimates of plutonium recovery based on kinetic desorption experiments described in Reimus et al. (2000b) suggest that it is unlikely that plutonium would migrate in significant quantities over significant distances sorbed to colloids under the conditions of these fracture flow experiments.

Figures 6 and 7 present the same flow-through experiment data but the simulated breakthrough in Figure 7 was calculated using an $O_2(g)$ fugacity of 10^{-7} bars.¹⁴ This $O_2(g)$ fugacity was used in Cheshire HST simulations (Pawloski et al., 2001). The early breakthrough that results from colloid-facilitated transport is significantly attenuated at an $O_2(g)$ fugacity of 10^{-7} bars and does not compare favorably with data. Under these conditions, the model severely underestimates the role of colloids in plutonium transport.

The increase in plutonium concentration at later time (Figure 7) is a result of free plutonium breakthrough (i.e. not associated with colloids). Since the sorption of plutonium to fracture-lining and matrix minerals is significantly reduced at the higher $O_2(g)$ fugacity, migration of free plutonium is enhanced. This is not observed at an O_2 fugacity of 10^{-15} bars. The effect of plutonium oxidation state on transport will later be examined at simulation time scales more relevant to near-field transport at Pahute Mesa (Section 4). Nevertheless, these results suggest that Cheshire HST simulations underestimated the role of colloids on plutonium transport.

In Figures 9 and 10, simulations under-predicted the breakthrough of plutonium to some degree. The data in these figures relate to experiments performed at the slowest flow rates in which predicted diffusion of plutonium from the fracture to the matrix was the greatest. The under-predictions indicate that plutonium desorption from colloids may be kinetically controlled to a degree and slow enough to reduce plutonium migration into the matrix under slow-flow conditions. However, other processes may also affect downstream plutonium breakthrough in a similar way, as discussed earlier. A more controlled fracture flow experiment would be necessary to isolate the effect of desorption kinetics from the many other factors (such as D_e) which may affect these simulation results.

3.4 Breakthrough results for silica colloid flow-through experiments

Surface complexation modeling based on data in Pawloski et al. (2001) predicts that plutonium (both Pu(IV) and Pu(V)) sorbs much more weakly to silica colloids than observed in Reimus et al. (2000b) batch sorption experiments. For model predictions to match batch sorption experiments, the reactive surface area of the silica colloids would have to be set to an unrealistically high value, the surface complexation reaction constants would have to be adjusted by orders of magnitude, or the surface complexation reactions

¹⁴ All other simulations presented in Section 3 of this report were run at an $O_2(g)$ fugacity of 10^{-15} bars.

themselves would need to be reevaluated. The inability to simulate plutonium sorption to silica colloids results largely from the lack of published sorption data for plutonium on model silicate minerals (see Zavarin and Bruton, 2000b). While the sorption data presented in Reimus et al. (2000b) could be used to establish new estimates of surface complexation reaction constants, the data are too limited (only two solution conditions) to appropriately constrain surface complexation reaction constants. Additional laboratory investigation of plutonium surface complexation to silicate minerals in conjunction with published data are necessary to better calibrate the surface complexation model.

Notwithstanding the limitations of the surface complexation model for silica, the simulation results are in general agreement with breakthrough data: plutonium breakthrough in silica colloid experiments is significantly less than in the smectite case. In the low flow rate (1.5 mL/hr) experiment (Figure 15), breakthrough was neither measured nor predicted. By comparison with Figures 6 and 11 (similar experimental conditions but smectite colloids used), silica is clearly a weaker sorber. In the high flow rate (5 mL/hr.) experiment (Figure 16) plutonium breakthrough is underpredicted. However, the more significant difference between these simulation results and breakthrough data is that simulated plutonium breakthrough is dominated by free plutonium while data of Reimus et al. (2000b) suggests that all effluent plutonium is associated with silica colloids. This difference relates to the inability of the surface complexation model to adequately predict the behavior of plutonium sorption to silica colloids.

It is surprising that simulation results suggest that free plutonium can migrate unretarded through the fractured column in the high flow rate silica colloid experiment (Figure 16). Two factors account for this behavior. First, the flow rate is sufficiently fast such that plutonium diffusion into the matrix is limited. Second, the pulse of plutonium is sufficiently long such that plutonium-sorbing minerals at the fracture-matrix boundary do not have an adequate sorptive capacity to reduce the aqueous plutonium concentration in the fracture. The combination of these two factors allows for a small fraction of free plutonium to travel nearly unretarded through the fracture. While it is important to note that these simulation results are not in agreement with experimental data, they, nevertheless, suggest that free plutonium may travel seemingly unretarded under very high flow velocity conditions.

3.5 Summary of colloid-facilitated plutonium transport studies

The migration of tritium in the fracture flow experiments reported in Reimus et al. (2000b) could be modeled using a D_e based on the Archie's Law with a fitted exponent of $m = 1.3$ and uncertainty of $\text{Log}(D_e) \pm 0.5$. Colloid-facilitated reactive transport of plutonium could be modeled effectively in the smectite colloid case when the redox state and the colloid reactivity were adjusted to match the batch sorption experiments. The $\text{O}_2(\text{g})$ fugacity was reduced to 10^{-15} bars and the reactive site concentration of the colloids was increased by a factor of ~ 50 from the initial TEM-based estimate. The results suggest that colloid-facilitated plutonium transport can be described reasonably well

using an equilibrium sorption model. Desorption kinetics effects could explain some of the inconsistencies between predicted and experimental data. However, under Pahute Mesa flow velocity/residence time conditions, experimentally observed desorption kinetics would not be expected to significantly affect Pu transport. This would suggest that observations of Kersting et al. (1999) could only be explained by an irreversible or nearly-irreversible component to Pu sorption to colloids.

Batch silica colloid sorption experiments could not be matched by our surface complexation model without adjusting silica reactive surface areas to an unreasonably high value or adjusting surface complexation reaction constants. However, in fracture flow experiments, predicted plutonium breakthrough results matched experimental data approximately. Fracture flow simulation results suggest plutonium migration as the free aqueous species (not associated with colloids). This is contrary to observations of Reimus et al. (2000b) and suggests that this approximate fit to data is, in part, coincidental.

Colloid breakthrough could not be effectively modeled because a colloid filtration mechanism was absent from the model. The addition of a colloid filtration model could properly capture the colloid breakthrough but would deteriorate the match between measured and modeled plutonium breakthrough; a combination of plutonium desorption kinetics, colloid reactive site concentration, plutonium diffusivity, and/or plutonium sorption to fracture-lining minerals would need to be further adjusted to match colloid and plutonium breakthrough simultaneously. While this could be done, we chose to evaluate these data in the context of the model used in Cheshire HST simulations (Pawloski et al., 2001) which did not include colloid filtration or sorption kinetics.

4 EVALUATION OF CHESHIRE HST FRACTURE-FLOW MODELING

In the following section, the role of colloids and matrix diffusion in plutonium reactive transport at the near-field scale (500 meters) is evaluated. Matrix diffusion and colloid-facilitated plutonium transport is evaluated in four separate modeling scenarios. These scenarios are meant to (1) compare breakthrough based on the Cheshire HST fracture flow conceptualization to an explicit parallel-plate fracture conceptualization, (2) evaluate the effect of matrix diffusion on tracer and plutonium transport at a near-field scale, and (3) evaluate the effects of plutonium redox and colloid reactivity on plutonium transport. However, the simulations are all based on a fracture-flow environment similar to that of the Cheshire near-field and are not meant to be extrapolated to fracture-flow in general.

4.1 Modeling scenarios

In the first modeling scenario (Cheshire 1D simulations), we revisit the 1D simulation results presented in Appendix I.4 of Pawloski et al. (2001). These 1D simulations entail the flow of source term radionuclides from 100 meters of a simulated cavity zone through

500 meters of a high permeability fracture zone. The simulations did not include matrix diffusion and treated the fracture porosity as a bulk effective porosity. The effective porosity of the fractured medium was based on a conceptual model developed in Chapter 6 of Pawloski et al. (2001) in which the effective porosity was computed from a fracture density of 8 per meter and an associated “matrix reactive zone” of 2.5 mm along each fracture (Figure 17). This conceptualization was necessary to merge the effective porosities established by the hydrologic and geochemical models. The conceptualization was used in the particle and streamline simulations presented in Chapter 7 of Pawloski et al. (2001).

In the second modeling scenario (Figure 18, Case A), we develop a new simulation in which fracture, fracture-lining minerals, and matrix minerals are explicitly modeled in a 2D simulation. The dimensions of this explicit fracture model are equivalent to the 1D effective porosity conceptualization developed in Chapter 6 and Appendix I of Pawloski et al. (2001), with a 0.25 mm fracture half-aperture, a 0.1 mm fracture-lining, and 2.5 mm “matrix reactive zone”. Flow is allowed in all three components and the net flux is consistent with the ~1 meter/year Darcy flux used in Appendix I of Pawloski et al. (2001). The 1 m/year Darcy flux results in a 100 m/year fluid velocity in the Appendix I simulations; this velocity is honored in the Case A simulation. Diffusion between the fracture, fracture-lining, and matrix reactive zone is set high enough to allow for complete mixing between these zones. The results from Case A are used to test whether the abstracted “effective porosity” conceptualization of fracture flow used in the Cheshire simulations is equivalent to this explicit single fracture simulation.

In the third modeling scenario (Figure 18, Case B), we use the identical model geometry as Case A but allow flow only within the fracture. Additionally, we set D_e for radionuclide migration into the fracture-lining and the 2.5 mm matrix zone based on simulation fits discussed earlier. To adhere to the original fluid flux used in previous simulations, the flow velocity in the fracture is increased appropriately. Thus, the fluid fluxes through the simulated fractures in Case A and Case B are equivalent. Case A and Case B results can be compared to evaluate the difference in breakthrough for a *flowing* “matrix reactive zone” conceptualization versus a *diffusion-only* matrix zone conceptualization.

In the fourth modeling scenario (Figure 18, Case C), we evaluate the effect of matrix diffusion and colloid facilitated plutonium transport for a simulation in which the full volume of the matrix is available for diffusion, instead of only 2.5 mm. Retaining the 8 per meter fracture density used in the Cheshire near-field model results in a matrix thickness of ~62.5 mm per half fracture. The effect of matrix diffusion and colloid facilitated transport on plutonium and tritium breakthrough are evaluated and compared to simulation results in Cases A and B.

The fracture-lining, matrix, and colloid mineralogy and mineral abundances used in all modeling scenarios (Table 1) are identical to those used in Cheshire HST simulations. The same fracture-lining and matrix mineralogy was used in the Section 3 models. The

colloid loads were equivalent to those used in the Cheshire simulations (5.91×10^{-6} mol/L $>\text{SiOH}$ and $>\text{AlOH}$ reactive site concentrations), significantly lower than those used to model the data of Reimus et al. (2000b). However, in this case, a steady-state concentration of colloids is allowed to travel through the simulated fracture instead of a pulse of colloids. Surface complexation reactions used in all simulations presented in this report are the same and based on the data in Zavarin and Bruton (2000a; 2000b).

4.2 Results and model comparisons

In Figure 19, the breakthrough of plutonium and tritium is plotted for the Cheshire 1D simulation case shown in Figure I.7 of Pawloski et al. (2001). Given the 100 meter/year fluid velocity and 500 meter length of the simulated fracture, tritium breakthrough should occur at 5 years. Numerical dispersion in the CRUNCH code produces early breakthrough of trace quantities of tritium at a much earlier time. However, when simulations are examined on a linear scale, the 0.5 C/Co position is, in fact, at 5 years (Figure 20). Based on the 5 year tracer breakthrough and a 319 year plutonium breakthrough, the retardation factor for plutonium in this simulation is 64 (see Figures 20 and 21).

Figures 20 and 21 compare the plutonium and tritium breakthrough in the Cheshire 1D simulation case with the 2D single fracture Case A. Tailing in the 1D tritium breakthrough simulation is more severe than in the 2D case (Figure 20). This results from a combination numerical dispersion and a slight difference in the modeling grid. However, in the absence of numerical dispersion, the results would be identical. Numerical dispersion errors are much less significant when retardation is significant. Thus, in the case of plutonium (Figure 21), breakthrough in the Cheshire 1D simulation case and the 2D single fracture Case A is essentially identical. With the exception of numerical dispersion errors, Figures 20 and 21 indicate that our 1D and 2D (Case A) fracture flow conceptualizations are equivalent.

Tritium breakthrough for Cases A, B, and C is plotted in Figure 22. A significant finding is that the nominal D_e uncertainty of $\text{Log}(D_e) \pm 0.5$ that was based on diffusion cell experiments has little effect on tritium breakthrough for Cases B or C (breakthrough based on $\text{Log}(D_e) \pm 0.5$ were not plotted here because the results would be indistinguishable from the average D_e case). This results from a) the high fracture density of the simulated medium, b) the relatively slow flow velocity (100 meters/year), and c) the scale of the simulation. In Case C, the high fracture density used in this model is such that only 6.35 cm of fracture lining and matrix is available for diffusion for each half-fracture. Based on the diffusive penetration thickness, η , defined by Neretznicks (1980):

$$\eta = \frac{2}{\pi^{1/2}} (D_e t)^{1/2}, \quad (4)$$

the entire 6.35 cm of fracture lining and matrix could be penetrated by tritium in less than 193 days. In contrast, the 500 meters of fracture will take nearly ten times longer for

tritium to penetrate (500 meter model, 100 m/y fluid velocity). In effect, the matrix becomes fully saturated with respect to tritium at a similar or faster rate than the transport of tritium along the fracture. Thus, the particular D_e value has little effect on breakthrough.

Another important result is that the conceptualization of the flowing “matrix reactive zone” (Case A) is entirely equivalent to simulations in which flow is isolated to the fracture but *diffusion* into the “matrix reactive zone” is allowed (Case B). Tritium breakthrough results for these two simulations are identical (Figure 22). As pointed out in Chapter 6 of Pawloski et al. (2001), the 2.5 mm matrix reactive zone is equivalent to a 24 hour diffusive penetration thickness, η , as defined by Neretnicks (1980). The penetration of 2.5 mm of matrix is nearly instantaneous compared to the five years it takes the fluid to reach the end of the 500 meter simulated fracture. The conceptualization of the flowing “matrix reactive zone” is, therefore, equivalent to simulating fracture flow in which a 2.5 mm zone at the fracture-matrix boundary is accessible via diffusion.

In Case C, tritium breakthrough is significantly retarded when compared to Cases A and B. The breakthrough is retarded by a factor of ~ 10 . Thus, the matrix provides a significant sink to tritium. While uncertainty in D_e has little effect on tritium breakthrough in these simulations, accessibility of the matrix to diffusion will play an important role in retarding tracers.

Plots of plutonium breakthrough for Cases A, B, and C are shown in Figure 23. For each case, three simulations were run. In the first simulation, the chemistry of the system was equivalent to that in Cheshire HST simulations. In the second, the $O_2(g)$ fugacity was decreased from 10^{-7} to 10^{-15} bars to increase Pu association with colloids. As discussed earlier, lowering the $O_2(g)$ fugacity increases plutonium sorption to colloids as well as the plutonium-sorbing fracture-lining and matrix minerals. Finally, to further increase the fraction of plutonium sorbed to colloids, the reactive site density on the colloids was increased by a factor of 10. In this case, 90% of the plutonium in the fluid was associated with colloids. This level of plutonium-colloid association is equivalent to the level of association found in the synthetic colloids in the fracture flow experiments of Reimus et al. (2000b).¹⁵ It is also consistent with observations of Kersting et al. (1999).

For all simulations, results for Cases A and B are entirely equivalent. This is consistent with the tritium results discussed above. At the high $O_2(g)$ fugacity for Cases A and B, the retardation of plutonium relative to tritium is 64, equivalent to the retardation observed in 1D Cheshire HST simulations. When the $O_2(g)$ fugacity is lowered to 10^{-15} bars, sorption to the colloids and the fracture-lining and matrix minerals increases. For Cases A and B, the capacity of the fracture-lining and matrix minerals to sorb plutonium

¹⁵ The initialization of these simulations resulted in some variation in the background concentrations of plutonium. These result from the interaction of colloids in the fracture with the initial plutonium concentrations in the matrix. The highest background plutonium concentration in the simulations was 10^{-19} mol/L; this is well below what we consider to be background concentrations (see Thompson et al. (1999)).

is greater than the colloids. This results in a significant increase in plutonium retardation (retardation increases by a factor of 4.5). When the site density of the colloids is increased by a factor of 10, the sorptive capacity of the colloids is large enough to compete with fracture-lining and matrix minerals for plutonium. Under these conditions, the retardation of plutonium decreases to a level nearly equivalent to the high $O_2(g)$ fugacity simulation (retardation ~ 70).

As in the case of tritium, Case C results in significantly greater retardation than Cases A or B. In the high $O_2(g)$ fugacity simulation, breakthrough begins at 525 years as compared to 125 years for Cases A and B. In the low $O_2(g)$ fugacity simulation, plutonium does not breakthrough over the 1000 year simulation. As in the Case A and B simulations, a 10-fold increase in the reactive site density of the colloids results in simulated breakthrough similar to the high $O_2(g)$ fugacity simulation.

In nearly all the cases presented here, the uncertainty in the diffusion coefficient developed from the data of Reimus et al. (2001) was not found to be significant to the breakthrough of plutonium or tritium. However, in one case, the effect of the uncertainty in the diffusion coefficient was observable in the breakthrough data (Figure 24). In the simulation where the reactivity of the colloids was greatest (low $O_2(g)$ fugacity and high colloid reactivity) and the entire matrix was available for diffusion (Case C), the uncertainty in initial breakthrough resulting from the uncertainty in D_e was ± 100 years. When compared to the uncertainties associated with the reactivity of the colloids and redox state of plutonium, the uncertainty in diffusion coefficient is not of primary concern. It is, however, important to emphasize that under differing fracture conditions (e.g. low fracture densities), the uncertainty in the effective diffusion may have a more pronounced effect.

4.3 Summary of Cheshire HST fracture-flow modeling

The “matrix reactive zone” used in the Cheshire HST model to merge the effective porosities of the hydrologic and geochemical models results in reactive transport behavior equivalent to an explicit fracture flow model that includes diffusion but no flow within the “matrix reactive zone”. This occurs because the flow velocities are slow enough to allow for diffusive exchange between the flowing fracture and the small “matrix reactive zone”.

Under the geochemical conditions used in Pawloski et al. (2001), plutonium sorbs to colloids weakly and colloid-facilitated plutonium transport is not significant. When the sorptive strength of the colloids is adjusted (lowered $O_2(g)$ fugacity and increased reactive site density) to produce 90% colloid-associated plutonium, colloid-facilitated plutonium transport is significant but the enhanced plutonium transport is buffered by sorption to fracture-lining minerals. The resulting plutonium breakthrough is similar to plutonium breakthrough under the conditions used in Pawloski et al. (2001). However, lowering the $O_2(g)$ fugacity alone results in significantly greater plutonium retardation. At 8 fractures per meter, matrix diffusion can significantly retard tritium breakthrough ($R \sim 10$) and

increase plutonium retardation by a factor of 4. These results suggest that the plutonium and tracer breakthrough results in Pawloski et al. (2001) are conservative but not inconsistent with the matrix diffusion and colloid-facilitated reactive transport data of Reimus et al. (2000a, 2000b).

5 CONCLUSIONS

Evaluation of the matrix diffusion and colloid-facilitated reactive transport data of Reimus et al. (2000a, 2000b) can be summarized by the following:

- Differences in D_v for ^3H , ^{14}C , and ^{99}Tc are insignificant when compared to the uncertainty in experimentally determined D_e .
- Subtle tracer-specific diffusion behavior such as ion exclusion is not significant when compared to the uncertainty in D_e .
- Processes other than diffusion (sorption, coprecipitation, etc.) play a minor role in ^{14}C and ^{99}Tc transport.
- D_e for all radionuclides can be modeled using the simple Archie's Law and a fitted exponent of $m = 1.3$.
- An uncertainty of $\text{Log}(D_e) \pm 0.5$ is consistent with the large uncertainties in the experimentally determined D_e .
- Tritium transport predicted using the Archie's Law fitted to data in Reimus et al. (2000a) matches well with tritium fracture flow data of Reimus et al. (2000b).
- Plutonium transport simulations match fracture-flow experiments when the redox state and the colloid reactivity are adjusted to match batch sorption experiments.
- Plutonium transport simulations could match fracture flow experiments with an equilibrium sorption model but some desorption kinetics effects may have been observed.
- Colloid breakthrough could not be effectively modeled because a colloid filtration mechanism was absent from our model.
- The "matrix reactive zone" used in the Cheshire model matches an equivalent simulation with an explicit fracture and diffusion-only exchange with the matrix.
- Matrix diffusion provides significant retardation to both tracers and sorbing radionuclides under Cheshire HST simulation conditions.

- Plutonium and tracer breakthrough results in Pawloski et al. (2001) are conservative but not inconsistent with the matrix diffusion and colloid-facilitated reactive transport data of Reimus et al. (2000a, 2000b).

6 RECOMMENDATIONS

We provide the following recommendations for future near-field and far-field modeling efforts:

- Matrix diffusion may significantly increase the retardation of sorbing and non-sorbing radionuclides if a significant quantity of matrix is accessible, and should be included in near-field models. An effective diffusion coefficient based on $D_e = D_v \phi^m$ where $m = 1.3$ should be used as a first approximation.¹⁶
- $\text{Log}(D_e) \pm 0.5$ effectively captures the uncertainty in the effective diffusion coefficients.
- The complex behavior of plutonium redox reactions needs to be further evaluated and more accurately modeled. Given the lack of available data at present, HST modeling should include a larger sensitivity analysis to possible redox states of aqueous and sorbed plutonium. $\text{O}_2(\text{g})$ fugacities ranging from 10^{-15} to 10^{-5} bars (region of Pu(V) dominance in solution) should be used to evaluate plutonium redox effects on transport.
- The use of the “matrix reactive zone” provides a simple method to merge hydrologic and geochemical models and does not affect breakthrough results when the zone is sufficiently narrow. However, the effect of the “matrix reactive zone” needs to be evaluated when the reactive zone thicknesses or fracture flow velocities differ significantly from those in this report.
- Additional sorption data are necessary for our surface complexation model to accurately predict plutonium sorption to silica.

7 REFERENCES

Drellack, S.L., Jr., Prothro, L.B., Roberson, K.E., Schier, B.A., Stevens, D.B. and Price, E.H., 1997. Analysis of Fractures in Volcanic Cores from Pahute Mesa, Nevada Test Site. DOE/NV/11718-160, Bechtel Nevada, Las Vegas, Nevada.

¹⁶ This recommendation is based on model fits to diffusion data for rocks examined in Reimus et al. (2000a; 2000b). Certain rocks at NTS may not fall within the range of characteristics (porosity, permeability, etc.) used in these calculations. In that case, the proposed equation may need modification.

- Duff, M.C., Hunter, D.B., Triay, I.R., Bertsch, P.M., Reed, D.T., Sutton, S.R., Shea-Mccarthy, G., Kitten, J., Eng, P., Chipera, S.J. and Vaniman, D.T., 1999. Mineral associations and average oxidation states of sorbed Pu on tuff. *Environmental Science & Technology*, 33(13): 2163-2169.
- Dullien, F.A.L., 1979. *Porous Media: Fluid Transport and Pore Structure*. Academic Press, Inc., San Diego, 396 pp.
- Giambalvo E.R., Steefel C.I., Fisher A.T., Rosenberg N.D., and Wheat C.G.(2001, submitted) Effect of fluid-sediment reaction on hydrothermal fluxes of major elements, eastern flank of the Juan de Fuca Ridge. *Geochimica et Cosmochimica Acta*.
- IT Corporation, 1998. Summary of Micrographic Analysis of Fracture Coating Phases on Drill Cores from Pahute Mesa, Nevada Test Site. DOE/NV/13052--050, IT Corporation, Las Vegas, Nevada.
- Keeney-Kennicutt, W.L. and Morse, J.W., 1985. The redox chemistry of Pu(V)O_2^+ interaction with common mineral surfaces in dilute solutions and seawater. *Geochimica et Cosmochimica Acta*, 49(12): 2577-2588.
- Kersting, A.B., Efur, D.W., Finnegan, D.L., Rokop, D.J., Smith, D.K. and Thompson, J.L., 1999. Migration of plutonium in ground water at the Nevada Test Site. *Nature*, 397(6714): 56-59.
- Mills, R. and Lobo, V.M.M., 1989. *Self-Diffusion in Electrolyte Solutions: A Critical Examination of Data Compiled for the Literature*. Physical Sciences Data 36. Elsevier, Amsterdam, 346 pp.
- Neretnicks, I., 1980. Diffusion in the rock matrix: An important factor in radionuclide retardation? *Journal of Geophysical Research*, 85(B8): 4379-4397.
- Nitsche, H. and Edelstein, N.M., 1985. Solubilities and speciation of selected transuranium ions. A comparison of a non-complexing solution with a groundwater from the Nevada Test Site. *Radiochimica Acta*, 39: 23-33.
- Nitsche, H., Gatti, R.C., Standifer, E.M., Lee, S.C., Muller, A., Prussin, T., Deinhammer, R.S., Maurer, H., Becraft, K., Leung, S. and Carpenter, S.A., 1993. Measured Solubilities and Speciations of Neptunium, Plutonium, and Americium in a Typical Groundwater (J-13) from Yucca Mountain Region. LA-12562-MS, Los Alamos National Laboratory, Los Alamos, New Mexico.
- Nitsche, H., Roberts, K., Prussin, T., Muller, A., Becraft, K., Keeney, D., Carpenter, S.A. and Gatti, R.C., 1994. Measured Solubilities and Speciations from Oversaturated Experiments on Neptunium, Plutonium, and Americium in UE-25p #1 Well

Water from the Yucca Mountain Region. LA-12563-MS, Los Alamos National Laboratory, Los Alamos, New Mexico.

- Pawloski, G.A., Tompson, A.F.B. and Carle, S.F., eds., 2001. Evaluation of the Hydrologic Source Term for Underground Nuclear Tests on Pahute Mesa and the Nevada Test Site: The Cheshire Test, Contributors: W.L. Bourcier, C.J. Bruton, S.F. Carle, J.I. Daniels, R.M. Maxwell, G.A. Pawloski, D.S. Shumaker, D.K. Smith, A.F.B. Tompson, and M. Zavarin. UCRL-ID-147023, Lawrence Livermore National Laboratory, Livermore, California.
- Reimus, P.W., Ware, S.D., Humphrey, A., Adams, A., Wilson, B., Gonzales, D., Warren, R.G. and Benedict, F.C., 2000a. Diffusive and Advective Transport of ^3H , ^{14}C , and ^{99}Tc in Saturated, Fractured Volcanic Rocks from Pahute Mesa, Nevada, Prepared for U.S. DOE, UGTA project, Los Alamos, New Mexico.¹⁷
- Reimus, P.W., Ware, S.D., Lu, N., Kung, S., Abdel-Fattah, A., Kersting, A., Hakem, N., Zhao, P. and Eaton, G., 2000b. Progress Report on Colloid-Facilitated Plutonium Transport in Fractured Rocks from Pahute Mesa, Nevada Test Site, Prepared for U.S. DOE, UGTA project, Los Alamos, New Mexico.
- Sanchez, A.L., 1983. Chemical Speciation and Adsorption Behavior of Plutonium in Natural Waters, University of Washington, Seattle, 191 pp.
- Sato, H. 1999. Matrix diffusion of simple cations, anions and neutral species in fractured crystalline rocks. *Nuclear Technology*, 129:199-210.
- Steeffel, C.I. (2000) New directions in hydrogeochemical transport modeling: Incorporating multiple kinetic and equilibrium reaction pathways. (L.R. Bentley, J.F. Sykes, C.A. Brebbia, W.G. Gray & G.F. Pinder, eds.) *Computational Methods in Water Resources XIII*, A.A. Balkema, Rotterdam, 331-338.
- Tompson, A.F.B., Bruton, C.J. and Pawloski, G.A., eds., 1999. Evaluation of the Hydrologic Source Term from the Underground Nuclear Tests in Frenchman Flat and the Nevada Test Site: The CAMBRIC Test, Contributors: W.L. Bourcier, C.J. Bruton, S.F. Carle, A.B. Kersting, G.A. Pawloski, J.A. Rard, D.E. Shumaker, D.K. Smith, and A.F.B. Tompson. UCRL-ID-132300, Lawrence Livermore National Laboratory, Livermore, California.
- Vaniman, D., Furlano, A., Chipera, S., Thompson, J. and Triay, I., 1995. Microautoradiography in studies of Pu(V) sorption by trace and fracture minerals in tuff. In: W.M. Murphy and D.A. Knecht (Editors), *Scientific Basis for Nuclear Waste Management XIX*. Material Research Society, Pittsburgh, pp. 639-646

¹⁷ A final version of this report was recently released by Los Alamos National Laboratory as report LA-13891-MS. The discussion presented in our report was based on the earlier progress report.

- Warren, R. G., D. A. Sawyer, F. M. Byers, Jr., and G. L. Cole, 2000. A Petrographic/Geochemical Database and Stratigraphic Framework for the Southwestern Nevada Volcanic Field. LA-UR-00-3791, Los Alamos National Laboratory, Los Alamos, New Mexico.
- Wolfsberg, A., Glascoe, L, Lu, G., Olson, A., Lichner, P., McGraw, M., and Cherry, T. 2001. TYBO/BENHAM: Model Analysis of Groundwater Flow and Radionuclide Migration from an Underground Nuclear Test in Southwestern Pahute Mesa, NTS. LA-UR-012924, Los Alamos National Laboratory, Los Alamos, New Mexico, May, 2001.
- Zavarin, M. and Bruton, C.J., 2000a. A Non-Electrostatic Surface Complexation Approach to Modeling Radionuclide Migration at the Nevada Test Site: Aluminosilicates. UCRL-ID-141840 DR, Lawrence Livermore National Laboratory, Livermore, California.
- Zavarin, M. and Bruton, C.J., 2000b. A Non-Electrostatic Surface Complexation Approach to Modeling Radionuclide Migration at the Nevada Test Site: Iron Oxides and Calcite. UCRL-ID-141841 DR, Lawrence Livermore National Laboratory, Livermore, California.

8 ACKNOWLEDGEMENTS

This work was funded by the Underground Test Area Project, U.S. Department of Energy, Nevada Operations Office, and performed under the auspices of the U.S. Department of Energy by the University of California, Lawrence Livermore National Laboratory under Contract No. W-7405-Eng-48.

Table 1. Radionuclide sorbing mineral abundances in the fracture linings and devitrified tuff used in the simulation of fracture flow experiments of Reimus et al. (2000b).[†]

Mineral	Average Volume %	Density Mg/m ³	Surface Area m ² /g
Mineral Abundances in the Fracture Linings §			
Iron Oxide (hematite)	2.15	5.28	2.0
Smectite	10.8	2.83	30.0
Calcite	7.09	2.71	2.2
Mineral Abundances in the Matrix			
Iron Oxide (hematite)	0.02	5.28	2.0
Smectite	0.25	2.83	30.0
Calcite	0	2.71	2.2

[†] Excerpted from Table 6.7 of Pawloski et al. (2001).

§ The average mineral composition of devitrified tuffs below the water table at Yucca Mountain also included 19.7% MnOx and 8.2% zeolites. Zeolites were ignored here because they are not expected to contribute significantly to plutonium sorption. Manganese oxides were ignored due to data limitations. See Pawloski et al. (2001) for more information.

Table 2. Parameters used in simulation of column flow-through experiments.

Experiment Number †	1a	2a	1b	2b	3a	4a	3b	4b	5a	6a	5b	6b
Figure Number †	2-11	2-13	2-12	2-14	2-15	2-17	2-16	2-18	2-19	2-21	2-20	2-22
Water Type	-----	Syn. WW-20 (2)	-----	-----	-----	WW-20 (3)	-----	-----	-----	WW-20 (4)	-----	-----
Flow Rate (mL/hr)	1.55	0.575	1.53	0.587	1.43	4.7	1.43	4.75	1.42	4.84	1.43	4.79
Injection Duration (hr)	7.73	24.4	7.52	23.4	16.4	5.23	16.3	5.18	10.07	4.6	9.78	4.42
Injected ³ H, cpm/g water	1069	1072	1069	651	669	3884	665	3884	2650	2220	2650	2220
Injected Pu, cpm/g water	296	456	296	393	396	389	399	389	678	506	678	506
Injected Pu, mol/L §	9.08E-9	1.4E-8	9.08E-9	1.21E-8	1.21E-8	1.19E-8	1.22E-8	1.19E-8	2.08E-8	1.55E-8	2.08E-8	1.55E-8
colloids, particles/mL	3.95E9	1.99E9	3.95E9	2.25E9	4.8E10	4.8E10	4.8E10	4.8E10	6.47E9	5.65E9	6.47E9	5.65E9
colloid diameter, nm ¶	-----	700.0	-----	-----	-----	100.0	-----	-----	-----	500.0	-----	-----
>>SiOH, mol/L ‡	1.2E-6	5.9E-7	1.2E-6	6.6E-7	5.8E-6	5.8E-6	5.8E-6	5.8E-6	9.7E-7	8.5E-7	9.7E-7	8.5E-7
>>AlOH, mol/L ‡	1.2E-6	5.9E-7	1.2E-6	6.6E-7	-----	-----	-----	-----	9.7E-7	8.5E-7	9.7E-7	8.5E-7
colloid type	-----	Ca-montmorillonite†	-----	-----	-----	-----	-----	-----	-----	Otay-montmorillonite†	-----	-----
Column	-----	2851	-----	2858	-----	2851	-----	2858	-----	2851	-----	2858
Length	-----	16.7	-----	21.9	-----	16.7	-----	21.9	-----	16.7	-----	21.9
Diameter	-----	-----	-----	-----	-----	8.7	-----	-----	-----	-----	-----	-----
pH	-----	8.50	-----	-----	-----	-----	-----	8.00	-----	-----	-----	-----
Na ⁺ , mol/L	-----	2.29E-3	-----	-----	-----	-----	-----	2.61E-3	-----	-----	-----	-----
Ca ²⁺ , mol/L	-----	-----	-----	-----	-----	-----	-----	1.80E-4	-----	-----	-----	-----
K ⁺ , mol/L	-----	3.37E-5	-----	-----	-----	-----	-----	3.32E-5	-----	-----	-----	-----
Mg ²⁺ , mol/L	-----	-----	-----	-----	-----	-----	-----	1.23E-5	-----	-----	-----	-----
SiO ₂ (aq)	-----	7.82E-4	-----	-----	-----	-----	-----	7.80E-4	-----	-----	-----	-----
HCO ₃ ⁻ , mol/L	-----	1.83E-3	-----	-----	-----	-----	-----	1.80E-3	-----	-----	-----	-----
SO ₄ ²⁻ , mol/L	-----	-----	-----	-----	-----	-----	-----	3.33E-4	-----	-----	-----	-----
Cl ⁻ , mol/L	-----	3.39E-4	-----	-----	-----	-----	-----	3.37E-4	-----	-----	-----	-----
F ⁻ , mol/L	-----	1.36E-4	-----	-----	-----	-----	-----	1.37E-4	-----	-----	-----	-----
NO ₃ ⁻ , mol/L	-----	2.42E-5	-----	-----	-----	-----	-----	2.42E-5	-----	-----	-----	-----
Fracture Aperture (cm);	-----	0.066	-----	0.044	-----	0.046	0.046	0.042	0.066	0.066	0.034	0.034
Fluid Velocity, m/yr	236	88	343	131	318	1045	343	1128	215	731	436	1476
Run Time, years	0.0221	0.0596	0.0224	0.0583	0.0239	0.0073	0.0239	0.0072	0.0241	0.0071	0.0239	0.0071
>>SiOH, mol/L ‡	6.0E-5	3.02E-5	6.0E-5	3.42E-5	5.8E-5	5.8E-5	-----	-----	5.01E-5	4.38E-5	5.01E-5	4.38E-5
>>AlOH, mol/L ‡	6.0E-5	3.02E-5	6.0E-5	3.42E-5	-----	-----	-----	-----	5.01E-5	4.38E-5	5.01E-5	4.38E-5

† From Reimus et al. (2000b).

§ Estimated value from information in Table 10-4 of Wolsberg et al. (2001).

¶ Estimated from TEM measurements in Reimus et al. (2000b).

‡ Reactive site concentrations for colloids calculated by method described in Zavarin and Bruton (2001a; 2001b). 2.31 sites/nm² for silica; 0.231 sites/nm² for smectite,

i From fits to tritium data performed in Reimus et al. (2001b).

‡ Adjusted colloid reactive site concentration used in model.

‡ Ca-montmorillonite and Otay-montmorillonite are two varieties of smectite mineral used in these experiments.

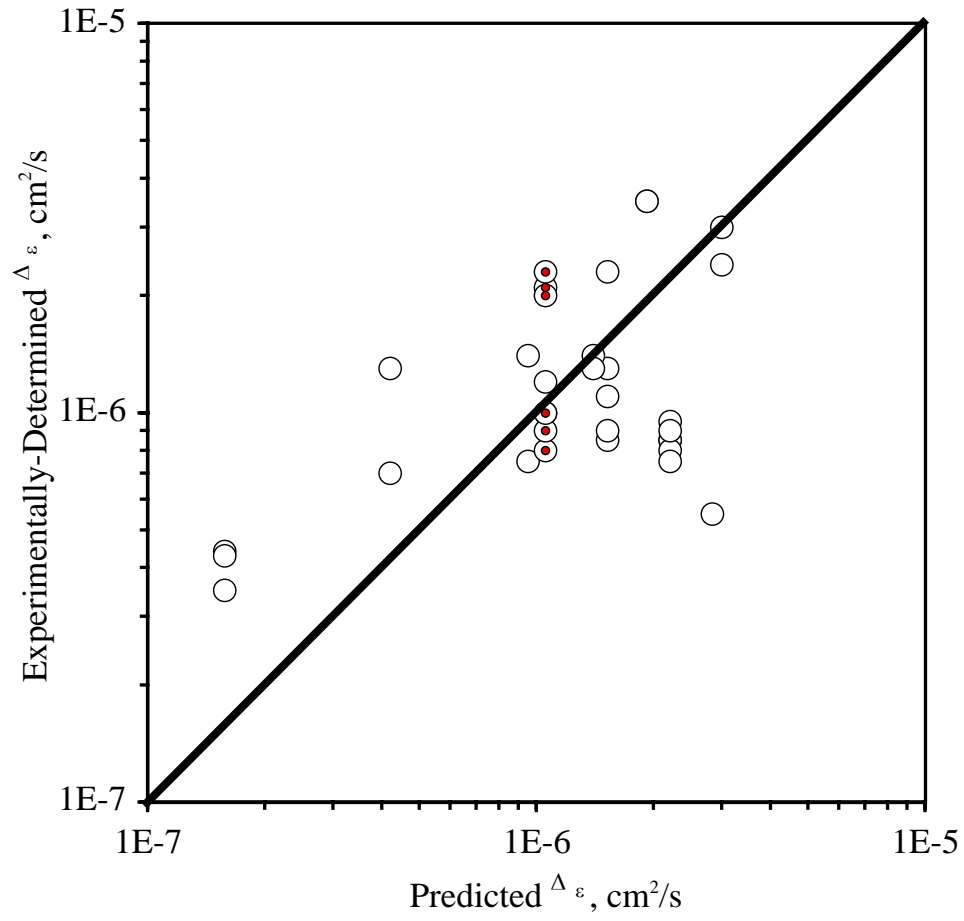


Figure 1. Correlation diagram between experimentally determined $\Delta \epsilon$ (diffusion cell data) and predicted $\Delta \epsilon$ based on Archie's law and $m = 1.7$. Red color denotes duplicate analyses of sub-samples from the PM2 4177 fractured rock sample.

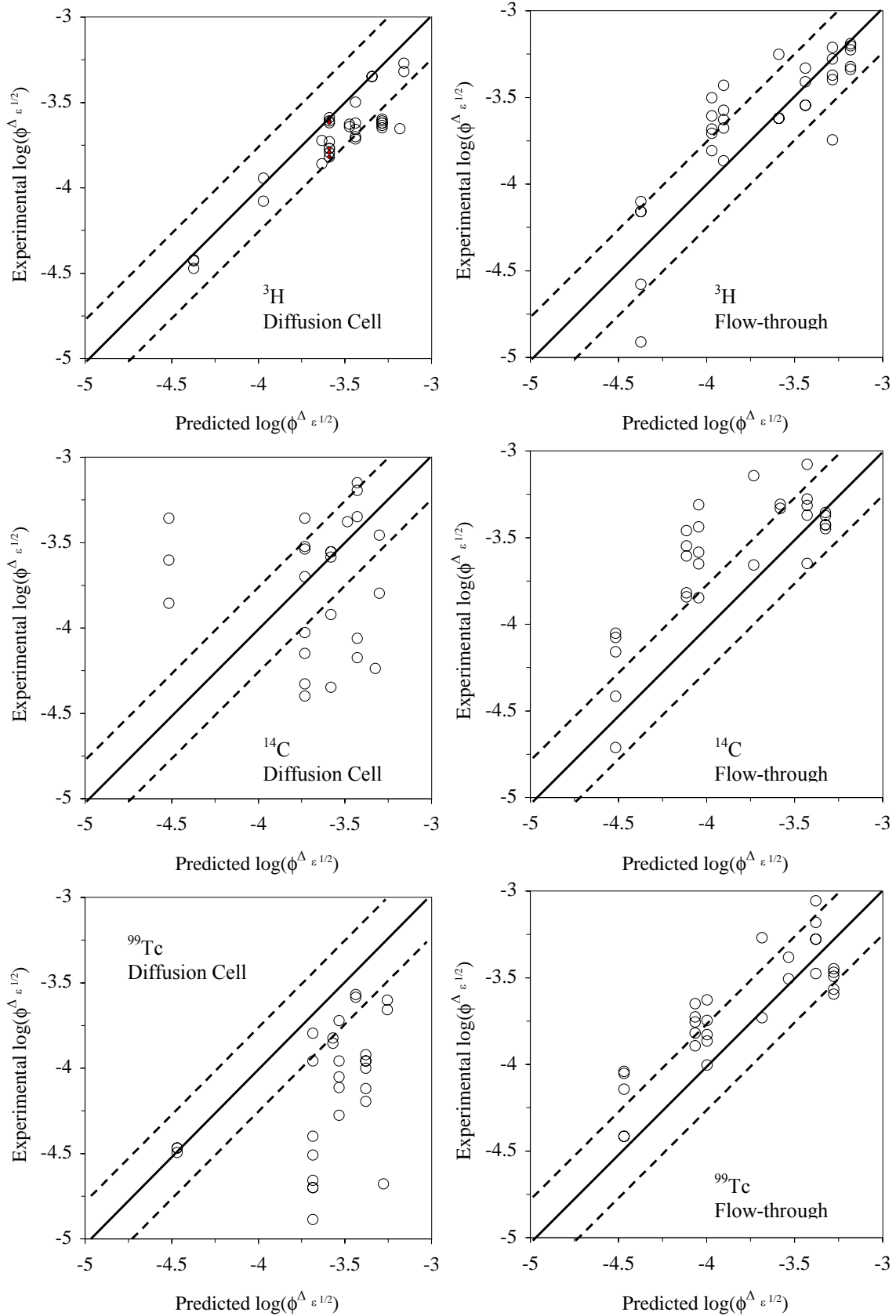


Figure 2. Correlation diagram between experimentally-determined and predicted matrix diffusion mass transfer coefficients (predicted Δ_e based on Archie's law and $m = 1.3$). Dashed lines indicate the $\text{Log}(D_e) \pm 0.5$ range.

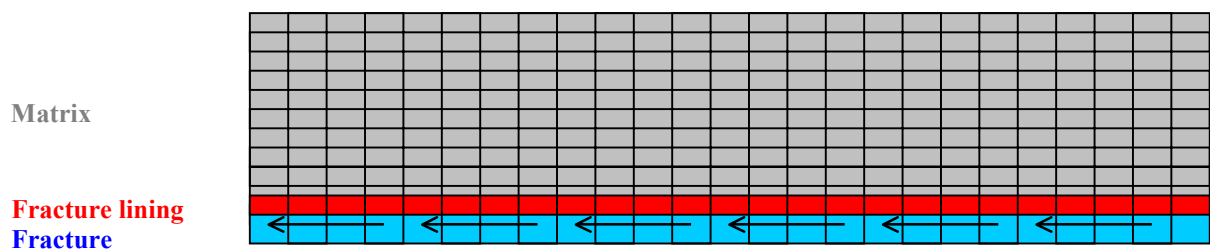


Figure 3. Grid used to simulate fracture flow utilizing data from fractured tuff flow-through columns of Reimus et al. (2000a). Grid blocks not to scale.

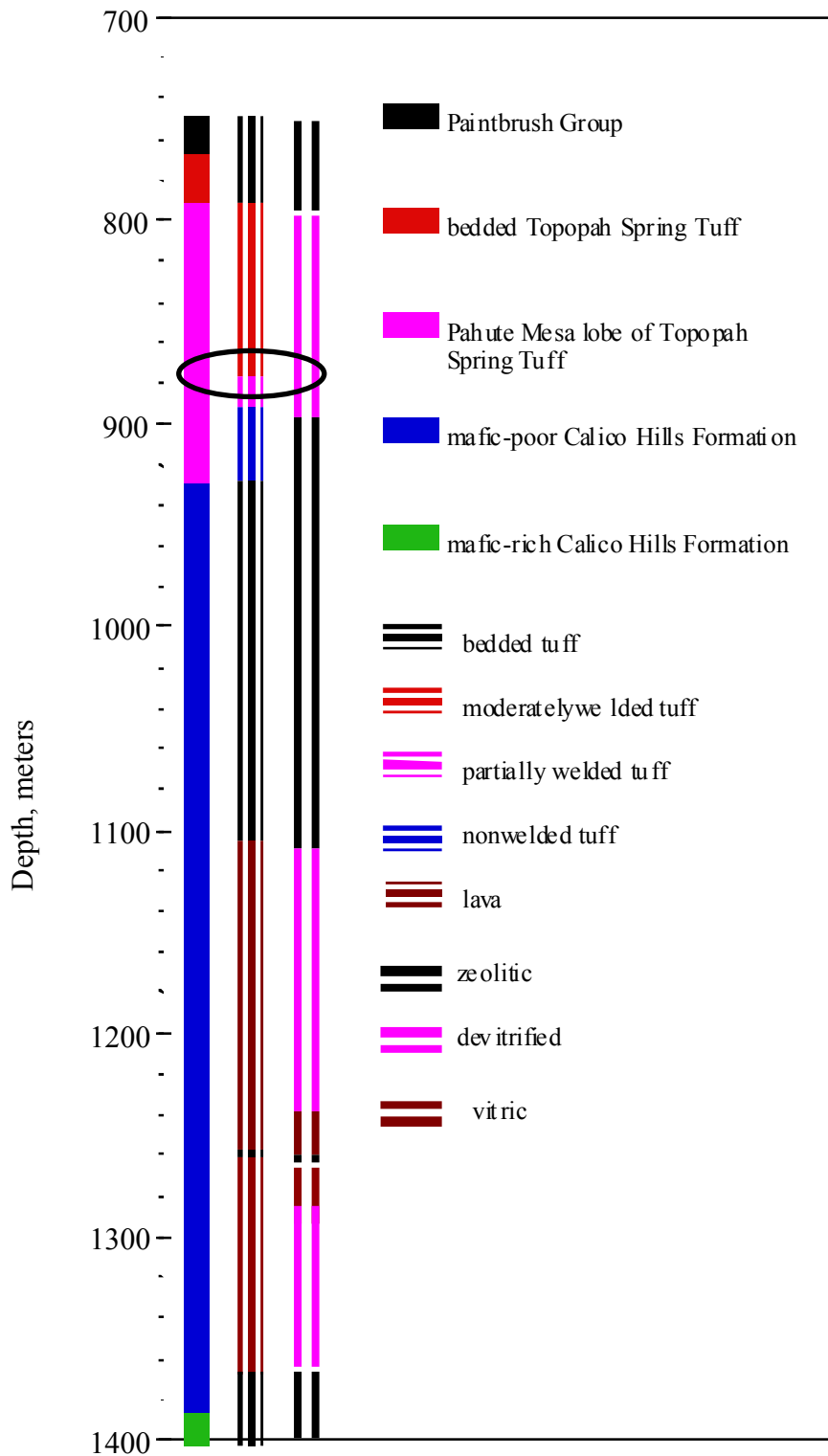


Figure 4. Stratigraphic unit, lithology, and alteration of tuffs from UE-20c. Circle indicates zone from which fractured tuff samples were taken for experiments reported in Reimus et al. (2000b). Data from Warren et al. (2000)

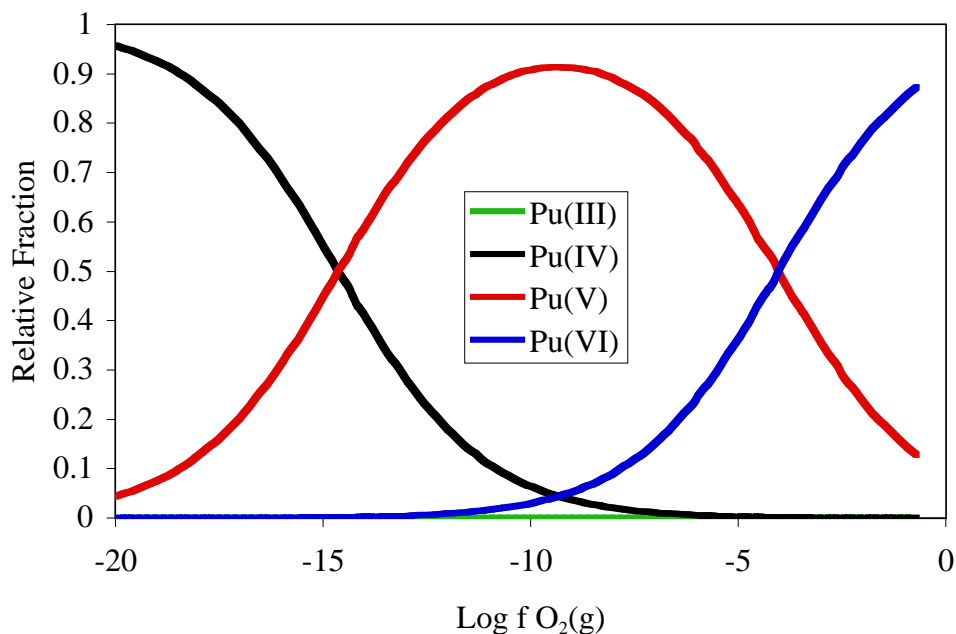


Figure 5. Relative fraction of plutonium oxidation states in J-13 type water as a function of $O_2(g)$ fugacity (bars) under equilibrium conditions.

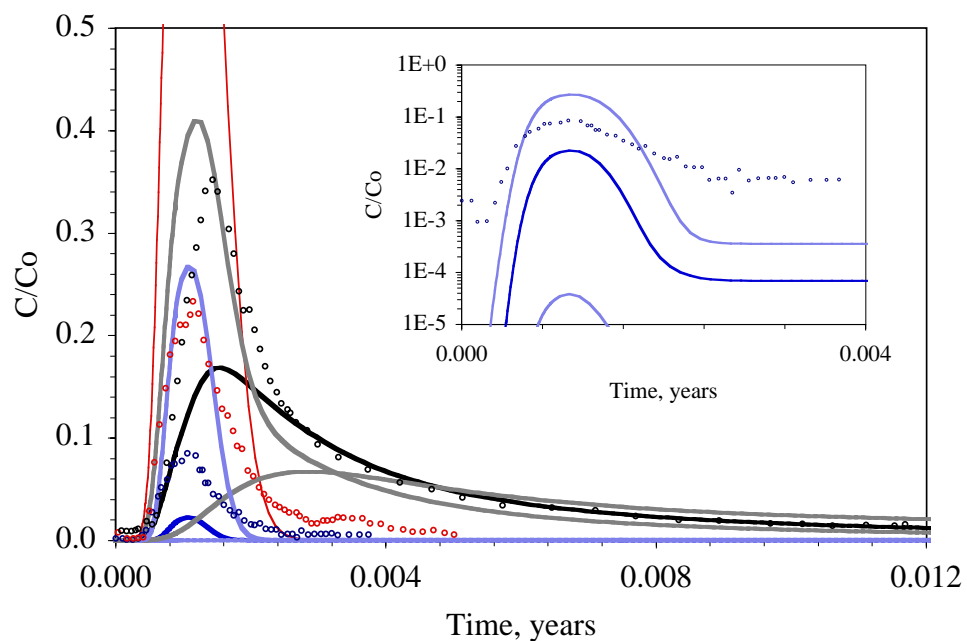


Figure 6. Experiment 1a (Figure 2-11 in Reimus et al., 2000b). Data points are breakthrough data for tritium (black), plutonium (blue), and clay colloids (red). Solid lines are simulation results using idealized diffusion coefficient (—) and $\text{Log}(D_e) \pm 0.5$ (—) at $O_2(g)$ fugacity = 10^{-15} bars (inset: Log-scale plutonium breakthrough).

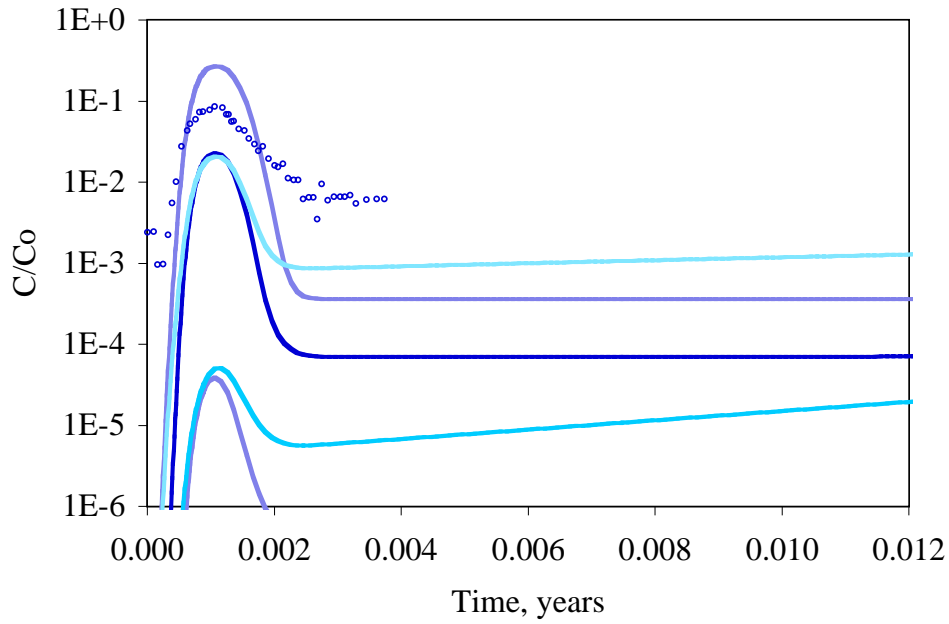


Figure 7. Experiment 1a (Figure 2-11 in Reimus et al., 2000b). Data points are breakthrough data for plutonium (blue). Solid lines are simulation results using idealized diffusion coefficient (—) at $O_2(g)$ fugacity = 10^{-7} bars (light blue) and 10^{-15} bars (blue) and $\text{Log}(D_e) \pm 0.5$ (—).

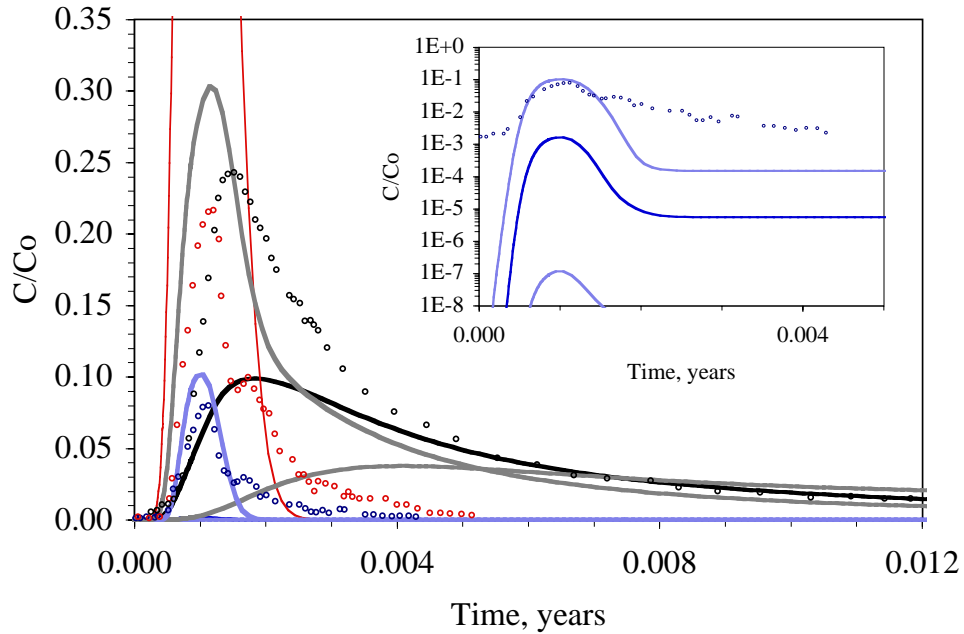


Figure 8. Experiment 1b (Figure 2-12 in Reimus et al., 2000b). Data points are breakthrough data for tritium (black), plutonium (blue), and clay colloids (red). Solid lines are simulation results using idealized diffusion coefficient (—) and $\text{Log}(D_e) \pm 0.5$ (—) at $O_2(g)$ fugacity = 10^{-15} bars (inset: Log-scale plutonium breakthrough).

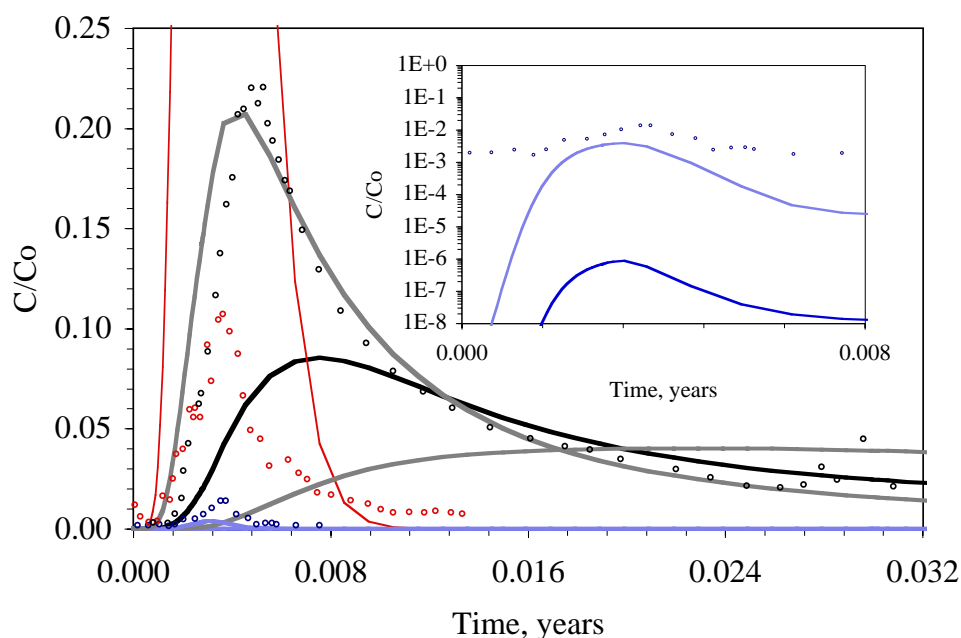


Figure 9. Experiment 2a (Figure 2-13 in Reimus et al., 2000b). Data points are breakthrough data for tritium (black), plutonium (blue), and clay colloids (red). Solid lines are simulation results using idealized diffusion coefficient (—) and $\text{Log}(D_e) \pm 0.5$ (—) at $\text{O}_2(\text{g})$ fugacity = 10^{-15} bars (inset: Log-scale plutonium breakthrough).

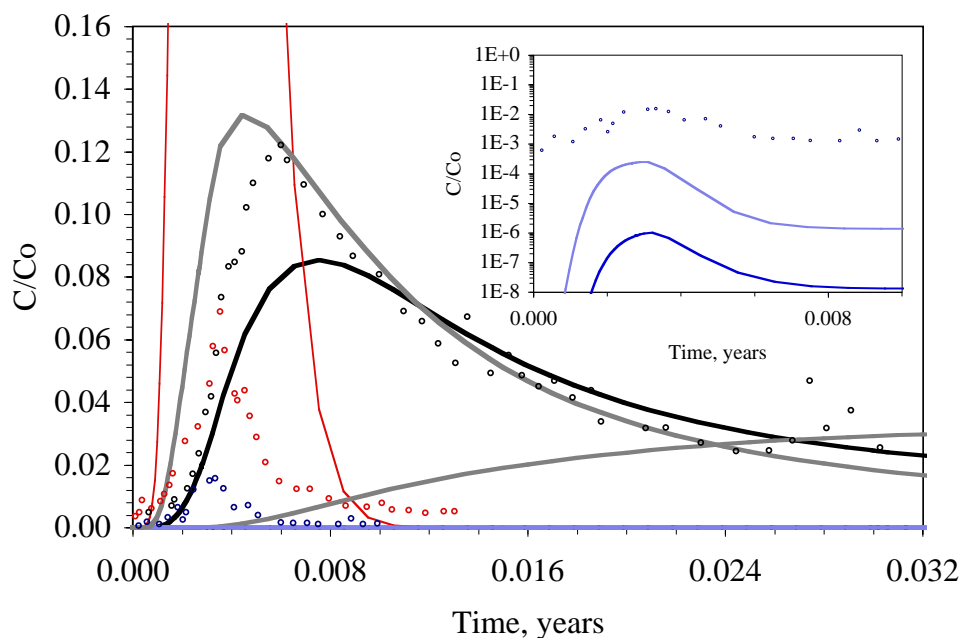


Figure 10. Experiment 2b (Figure 2-14 in Reimus et al., 2000b). Data points are breakthrough data for tritium (black), plutonium (blue), and clay colloids (red). Solid lines are simulation results using idealized diffusion coefficient (—) and $\text{Log}(D_e) \pm 0.5$ (—) at $\text{O}_2(\text{g})$ fugacity = 10^{-15} bars (inset: Log-scale plutonium breakthrough).

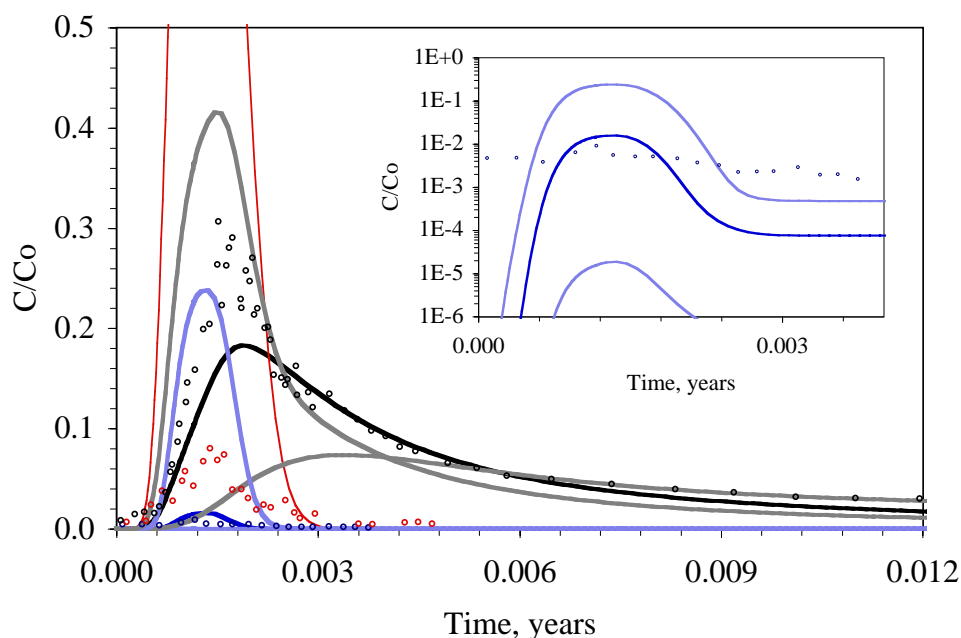


Figure 11. Experiment 5a (Figure 2-19 in Reimus et al., 2000b). Data points are breakthrough data for tritium (black), plutonium (blue), and clay colloids (red). Solid lines are simulation results using idealized diffusion coefficient (—) and $\text{Log}(D_e) \pm 0.5$ (—) at $\text{O}_2(\text{g})$ fugacity = 10^{-15} bars (inset: Log-scale plutonium breakthrough).

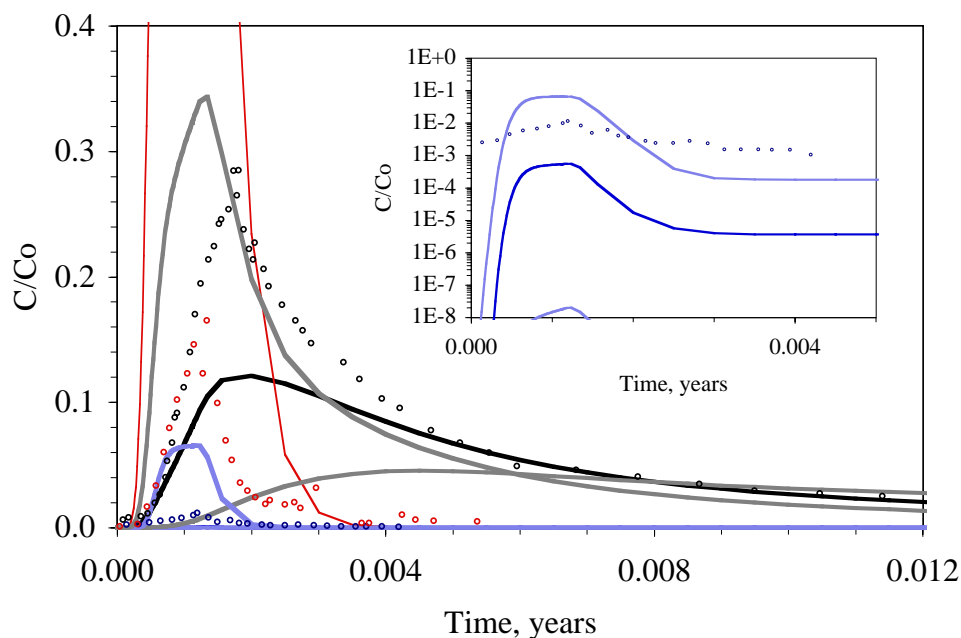


Figure 12. Experiment 5b (Figure 2-20 in Reimus et al., 2000b). Data points are breakthrough data for tritium (black), plutonium (blue), and clay colloids (red). Solid lines are simulation results using idealized diffusion coefficient (—) and $\text{Log}(D_e) \pm 0.5$ (—) at $\text{O}_2(\text{g})$ fugacity = 10^{-15} bars (inset: Log-scale plutonium breakthrough).

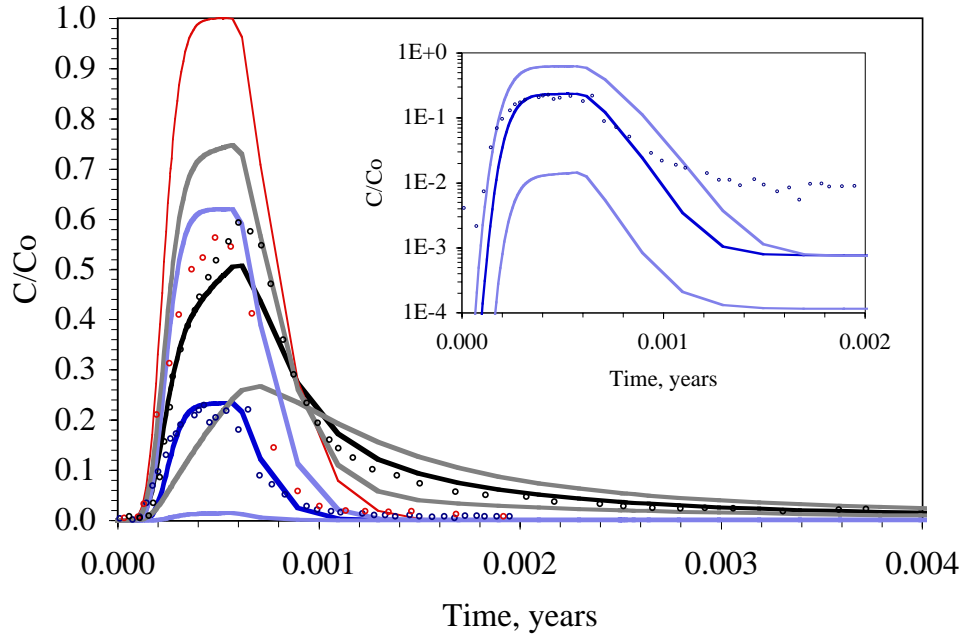


Figure 13. Experiment 6a (Figure 2-21 in Reimus et al., 2000b). Data points are breakthrough data for tritium (black), plutonium (blue), and clay colloids (red). Solid lines are simulation results using idealized diffusion coefficient (—) and $\text{Log}(D_e) \pm 0.5$ (—) at $\text{O}_2(\text{g})$ fugacity = 10^{-15} bars (inset: Log-scale plutonium breakthrough).

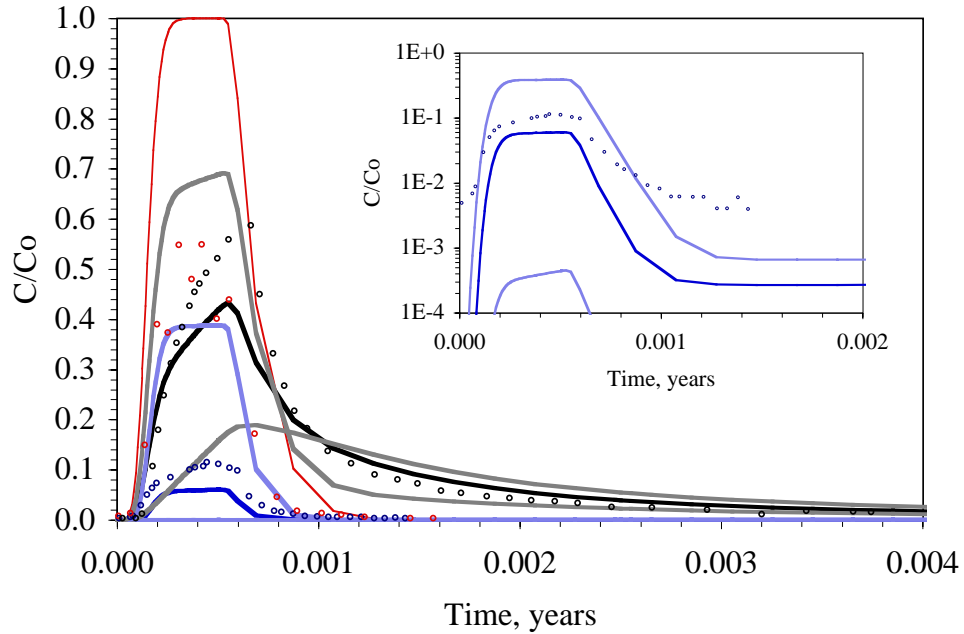


Figure 14. Experiment 6b (Figure 2-22 in Reimus et al., 2000b). Data points are breakthrough data for tritium (black), plutonium (blue), and clay colloids (red). Solid lines are simulation results using idealized diffusion coefficient (—) and $\text{Log}(D_e) \pm 0.5$ (—) at $\text{O}_2(\text{g})$ fugacity = 10^{-15} bars (inset: Log-scale plutonium breakthrough).

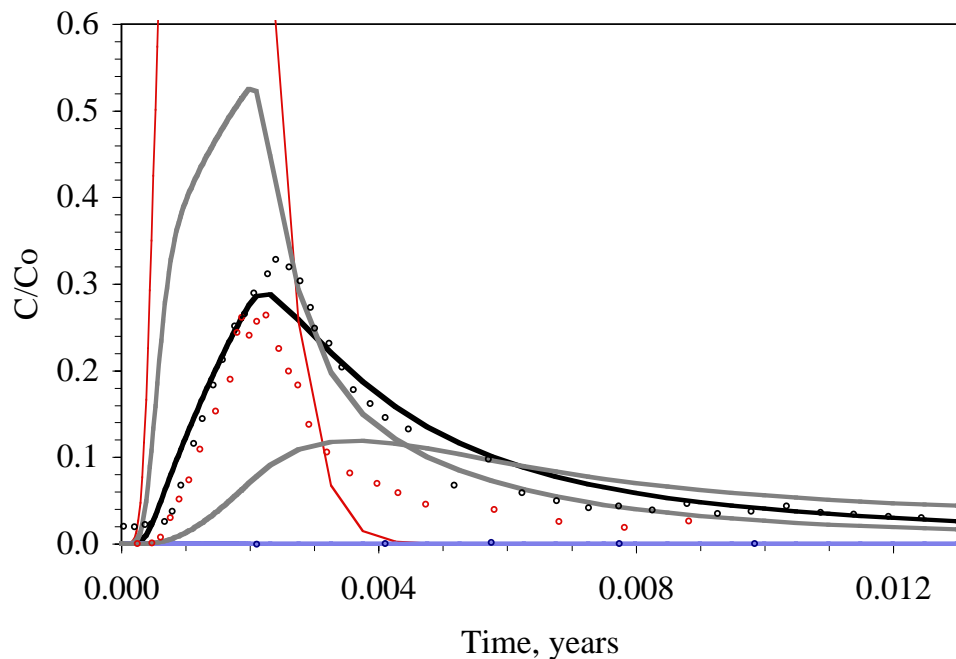


Figure 15. Experiment 3a (Figure 2-15 in Reimus et al., 2000b). Data points are breakthrough data for tritium (black), plutonium (blue), and silica colloids (red). Solid lines are simulation results using idealized diffusion coefficient (—) and $\text{Log}(D_e) \pm 0.5$ (—) at $\text{O}_2(\text{g})$ fugacity = 10^{-15} bars.

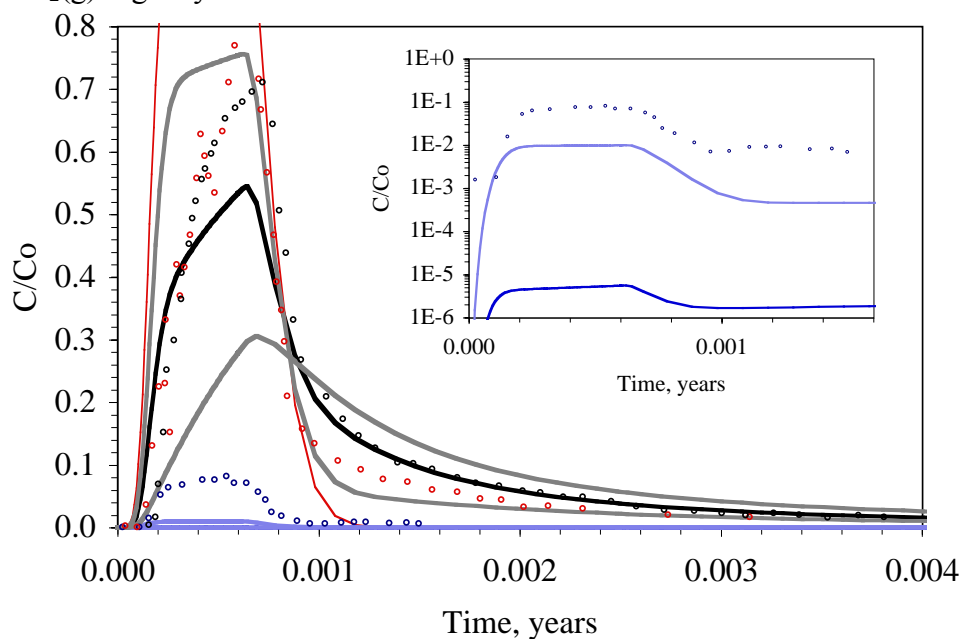


Figure 16. Experiment 4a (Figure 2-17 in Reimus et al., 2000b). Data points are breakthrough data for tritium (black), plutonium (blue), and silica colloids (red). Solid lines are simulation results using idealized diffusion coefficient (—) and $\text{Log}(D_e) \pm 0.5$ (—) at $\text{O}_2(\text{g})$ fugacity = 10^{-15} bars (inset: Log-scale plutonium breakthrough).

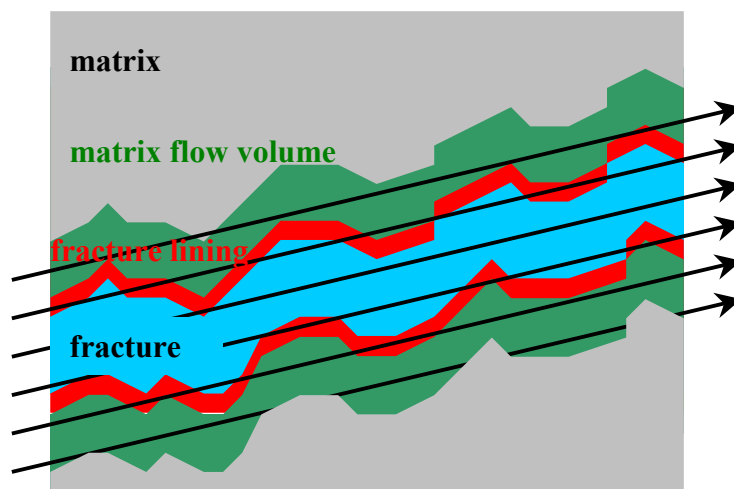
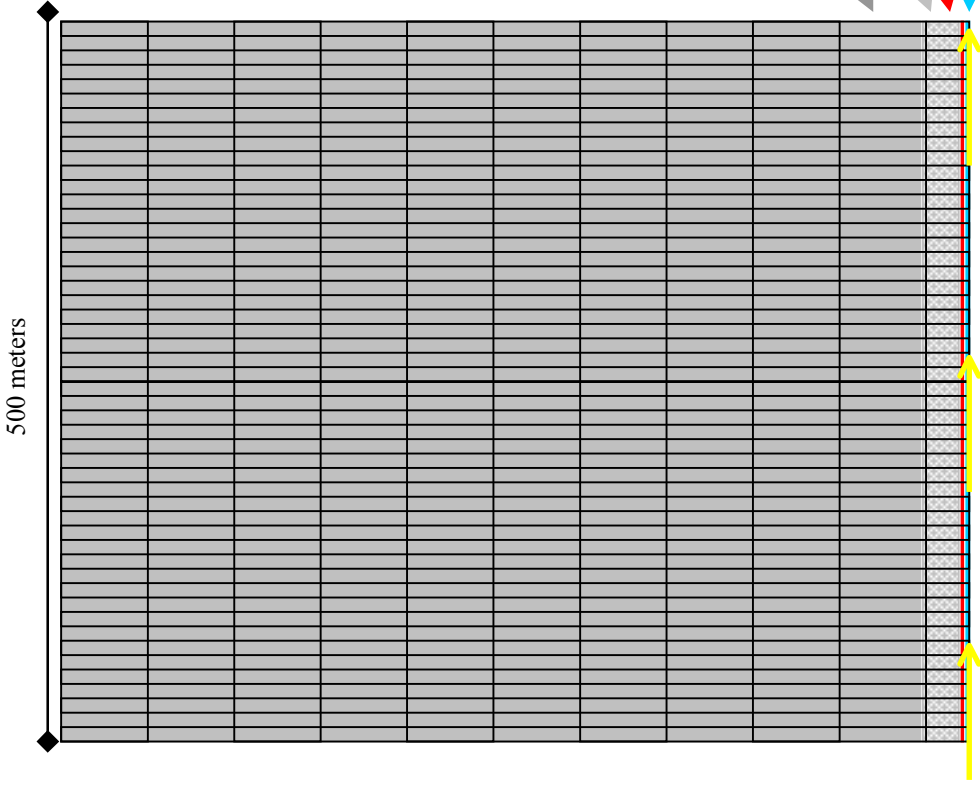


Figure 17. Figure 6.12 of Pawloski et al. (2001) showing the conceptual model used to define the nature of effective porosity and the interaction of radionuclides with fracture-lining minerals and matrix minerals.

Case C: Flow-through fracture only and diffusion into fracture lining and 62.5 mm matrix zone (8 fractures per meter equivalent).



Case A: Flow-through fracture, fracture lining, and 2.5 mm matrix zone as defined in Pawloski et al. (2001).



Case B: Flow-through fracture only and diffusion into fracture lining and 2.5 mm matrix zone.



Figure 18. Schematic of three types of flow simulations performed using the CRUNCH code.

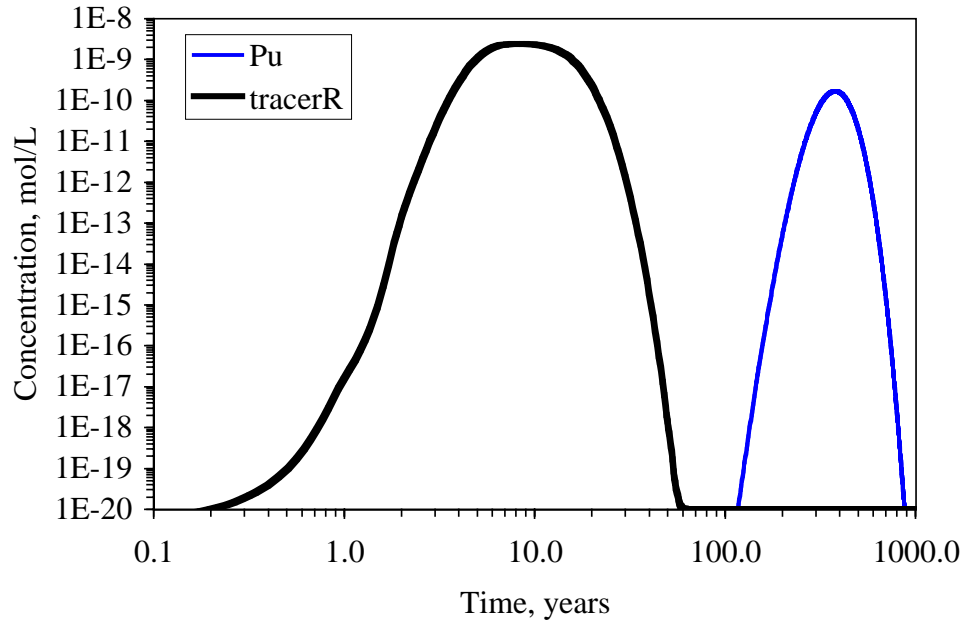


Figure 19. Breakthrough of plutonium and a tracer in the 1D simulations presented in Figure I.7 of Pawloski et al. (2001).

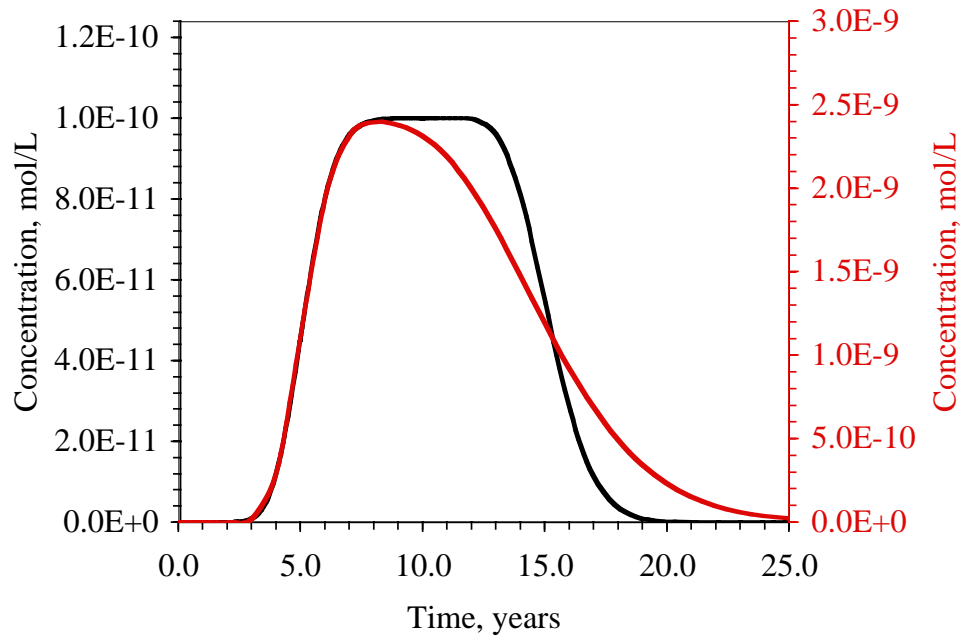


Figure 20. Breakthrough of tracer in the 1D simulation presented in Figure I.7 of Pawloski et al. (2001) (red) and Case A simulation (black). Linear scale indicates breakthrough at 5 years.

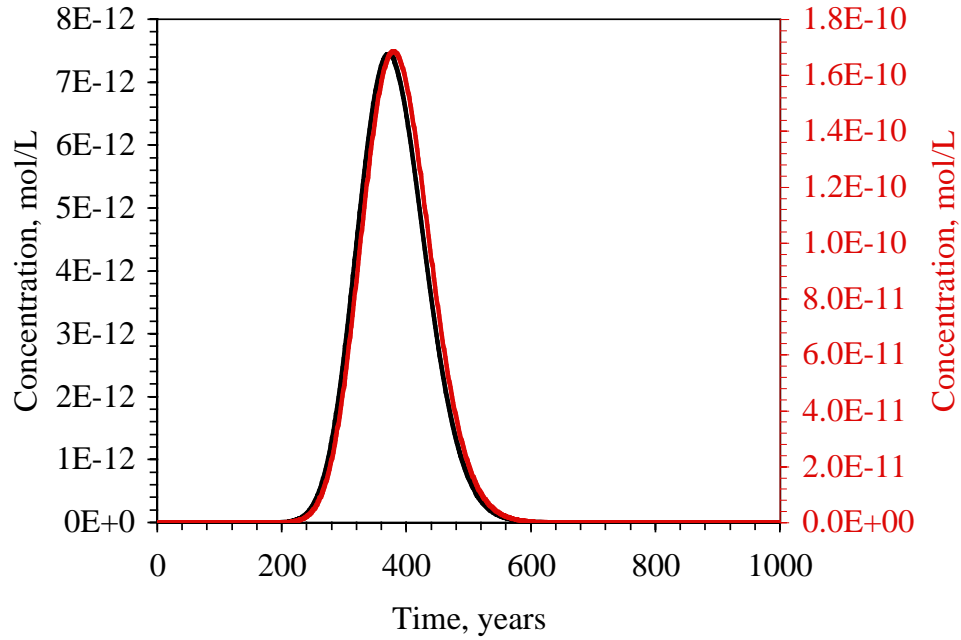


Figure 21. Breakthrough of plutonium in the 1D simulation presented in Figure I.7 of Pawloski et al. (2001) (red) and Case A simulation (black).

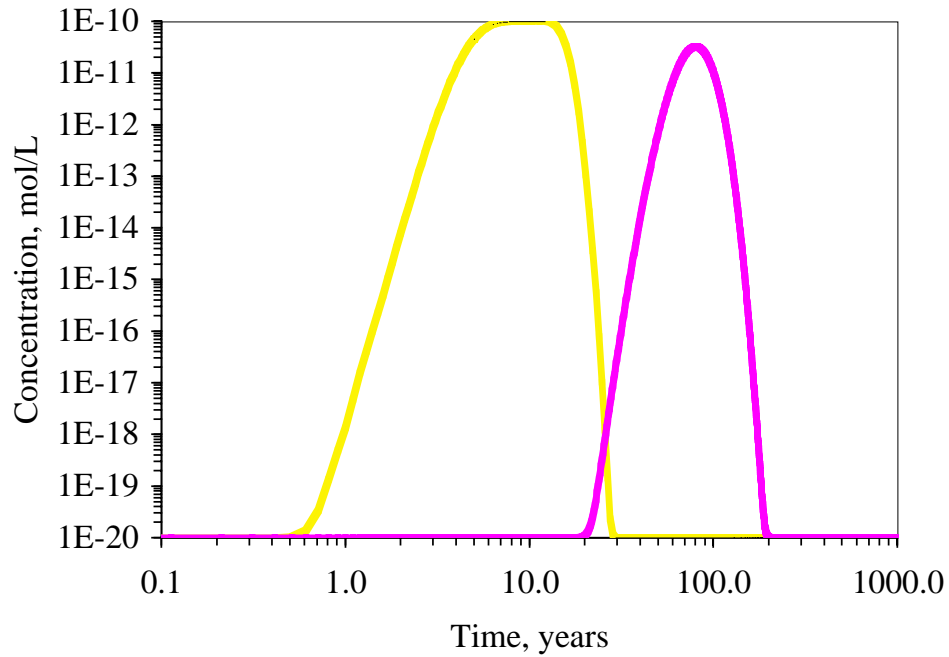


Figure 22. Breakthrough of tritium for Case A (yellow), Case B (black), Case C (pink).

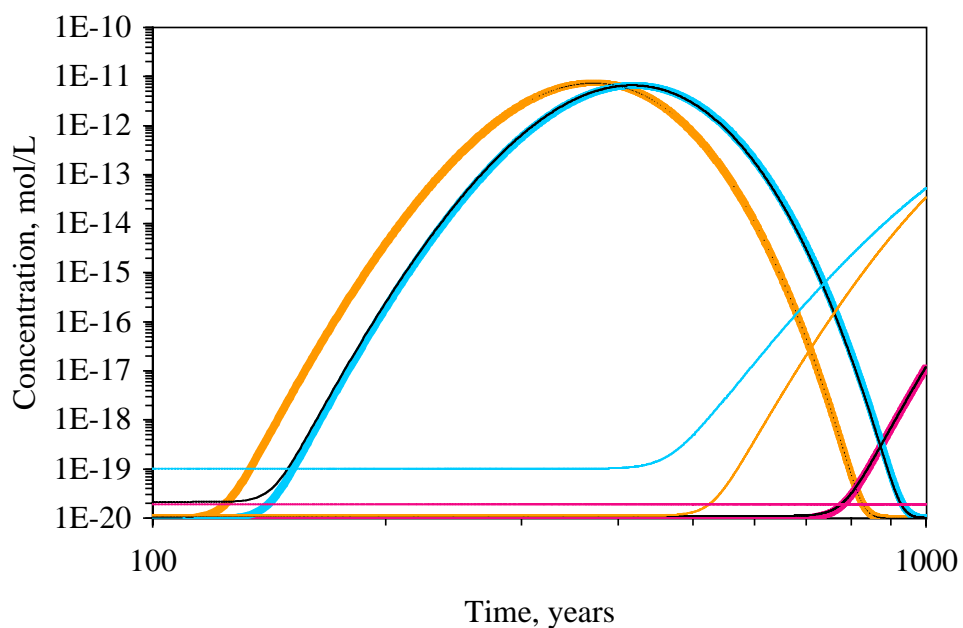


Figure 23. Breakthrough of plutonium for Cases A (colored thick lines), B (black lines), and C (colored thin lines) under conditions of $O_2(g)$ fugacity of 10^{-7} bars (orange), 10^{-15} bars (pink), and 10^{-15} bars and ten-fold increase in colloid reactivity (turquoise). Case B results in black.

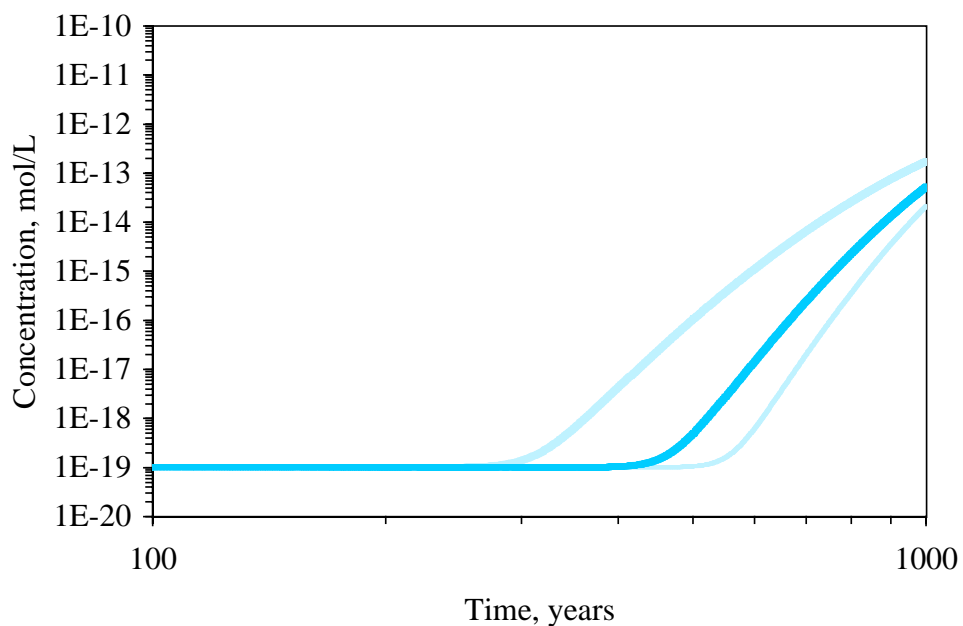


Figure 24. Breakthrough of plutonium in Case C in which $O_2(g)$ fugacity is 10^{-15} bars and colloid reactivity increased ten-fold. Light turquoise data show the effect of uncertainty in the diffusion coefficient.